Matter

CellPress
OPEN ACCESS

Article

Understanding and exploiting interfacial interactions between phosphonic acid functional groups and co-evaporated perovskites

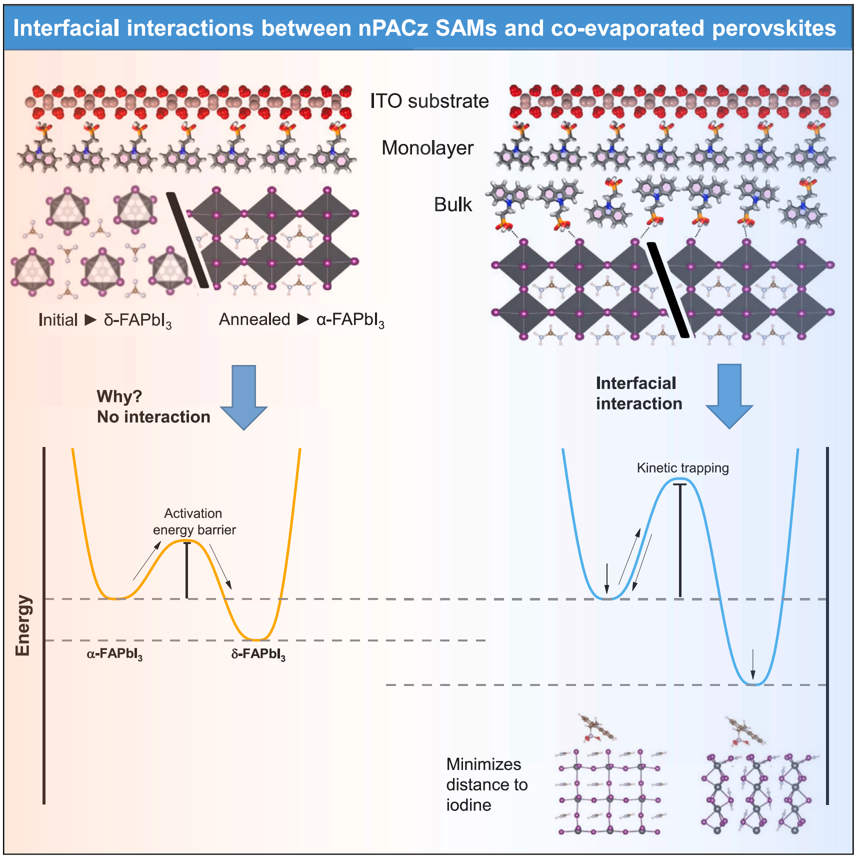

Thomas Feeney, Julian Petry, Abderrezak Torche, ..., Ganna Gryn'ova, Ulrich W. Paetzold, Paul Fassl

ganna.grynova@h-its.org (G.G.)
ulrich.paetzold@kit.edu (U.W.P.)
paul.fassl@kit.edu (P.F.)

Highlights

Expanding knowledge of substrate-dependent growth for co-evaporated perovskites

Understanding form of interfacial hydrogen bonding of nPACz molecules with iodine

Significant effect on organic incorporation rates and perovskite crystal structure

This work shows that nPACz self-assembled monolayer-based hole-transport layers are capable of hydrogen bonding with interfacial iodine in co-evaporated perovskites if bulk components are present. This interaction substantially shifts organic incorporation rates and initial perovskite crystal growth and can be controlled by intentional introduction of phosphonic acids. This opens the door for rational design of substrates to improve and tune perovskite growth and properties.

3

Understanding
Dependency and conditional studies on material behavior

Feeney et al., Matter 7, 1–25
May 1, 2024
https://doi.org/10.1016/j.matt.2024.02.004

Please cite this article in press as: Feeney et al., Understanding and exploiting interfacial interactions between phosphonic acid functional groups and co-evaporated perovskites, Matter (2024), https://doi.org/10.1016/j.matt.2024.02.004

Matter

CellPress
OPEN ACCESS

Article

Understanding and exploiting interfacial interactions between phosphonic acid functional groups and co-evaporated perovskites

Thomas Feeney,[1,2,9] Julian Petry,[1,2,9] Abderrezak Torche,[3,4] Dirk Hauschild,[5,6,7] Benjamin Hacene,[1] Constantin Wansorra,[5] Alexander Diercks,[1] Michelle Ernst,[3,4,8] Lothar Weinhardt,[5,6,7] Clemens Heske,[5,6,7] Ganna Gryn'ova,[3,4,*] Ulrich W. Paetzold,[1,2,*] and Paul Fassl[1,2,10,*]

SUMMARY

Interfacial engineering has fueled recent development of p-i-n perovskite solar cells (PSCs), with self-assembled monolayer-based hole-transport layers (SAM-HTLs) enabling almost lossless contacts for solution-processed PSCs, resulting in the highest achieved power conversion efficiency (PCE) to date. Substrate interfaces are particularly crucial for the growth and quality of co-evaporated PSCs. However, adoption of SAM-HTLs for co-evaporated perovskite absorbers is complicated by the underexplored interaction of such perovskites with phosphonic acid functional groups. In this work, we highlight how exposed phosphonic acid functional groups impact the initial phase and final bulk crystal structures of co-evaporated perovskites and their resultant PCE. The explored surface interaction is mediated by hydrogen bonding with interfacial iodine, leading to increased formamidinium iodide adsorption, persistent changes in perovskite structure, and stabilization of bulk α-$FAPbI_3$, hypothesized as being due to kinetic trapping. Our results highlight the potential of exploiting substrates to increase control of co-evaporated perovskite growth.

INTRODUCTION

Within the realm of emerging semiconductors for next-generation photovoltaic (PV) devices, organic-inorganic metal halide perovskite solar cells (PSCs) are promising.[1] They owe this to their tunable band gap coupled with high defect tolerance, absorption coefficients,[2] and carrier diffusion lengths.[3] While current certified power conversion efficiencies (PCEs) of planar inverted p-i-n PSCs lag behind their n-i-p counterparts,[4,5] the former possess several inherent advantages. These include their straightforward incorporation into monolithic tandem PV devices,[6,7] low-temperature fabrication requirements, minimal current-voltage hysteresis, and high operational stability.[4,8–11]

Absorber fabrication methods for PSCs can be roughly divided into two classes, i.e., solution processing and vacuum-based thermal evaporation.[12] Solution processing is the most ubiquitous method, encompassing spin coating, inkjet printing, slot-die coating, and dip coating.[13] Such techniques allow simple process optimization, require inexpensive equipment, and enable rapid absorber deposition. An alternative class of deposition methods for fabricating high-quality perovskite thin films is vacuum-based thermal evaporation (hereafter referred to as evaporation).

PROGRESS AND POTENTIAL

Evaporation is a promising and scalable fabrication method for the homogeneous deposition of perovskite thin films on industrially relevant areas. This work expands the current understanding of the critical role of the choice of substrate material for the growth of co-evaporated perovskite thin films. Specifically, we find that exposed phosphonic acid functional groups can impact the perovskite crystal structure and amounts of organic materials required for stoichiometric film growth. We reinforce our observations through computer simulations, material analysis, and X-ray spectroscopy to determine how these changes occur.

This study lays the groundwork for a controlled design of substrates to exploit such interfacial interactions. Substrate surfaces can be specifically designed to reduce the amount of required material to form perovskites while simultaneously improving the overall electrical properties of films. The results of this study have the potential to inform industry research in upcoming decades.

Please cite this article in press as: Feeney et al., Understanding and exploiting interfacial interactions between phosphonic acid functional groups and co-evaporated perovskites, Matter (2024), https://doi.org/10.1016/j.matt.2024.02.004

Compared to solution processing, evaporation is well suited to deposit on textured surfaces and readily maintains homogeneity over larger areas, leading to reduced upscaling losses for industrially relevant active areas.[14–16] Evaporated perovskites have seen a recent expansion into compositions traditionally only formed through solution processing, including triple-cation,[17] methylammonium (MA)-free, and wide-band-gap compositions.[18,19] Among these options, perovskites utilizing formamidinium (FA) halides as sole organic cations are particularly promising due to the expected improved performance and stability.[18]

The growth of co-evaporated perovskites shows a far greater dependence on a suitable choice of substrate compared to other fabrication methods, requiring optimized evaporation rates for good crystallization and device performance.[20–27] Olthof and Meerholz were the first to report that perovskite formation during co-evaporation exhibits a strong surface dependence that affects both film morphology and band alignment.[21] Many studies sought to understand this behavior, for example postulating catalytic decomposition for certain surfaces (such as TiO_2).[21,22] However, this is not sufficient to explain observed differences between catalytically inactive substrate materials. Abzieher et al. attempted a more universal explanation, observing changes in initial perovskite growth through suppression or incitement of Oswald ripening caused by substrate surface properties.[23] For inferior surfaces that result in non-optimal film morphology and low device performance, the initial formation of numerous small Pb-rich grains was observed, which tend to have reduced rates of organic cation incorporation.[22,23] A correlation was drawn between the substrate surface polarity (as determined by the water contact angle) and preferential initial crystal growth, highlighting that substrate-dependent initial growth conditions strongly influence bulk material properties. These observations were recently corroborated by Yan et al., who showed that co-evaporated perovskite film properties can be controlled on a variety of substrates by an ultrathin perovskite template layer deposited via prior separate sequential evaporation.[20]

Critically, surface-based functional group interactions add a further layer of complexity for surface-dependent growth, the clearest example being the co-evaporation of $FAPbI_3$ (formamidinium lead triiodide)-based absorbers on MeO-2PACz ([2-(3,6-dimethoxy-9*H*-carbazol-9-yl)ethyl]phosphonic acid) reported by Roß et al.[24] MeO-2PACz is a member of the nPACz family, a group of self-assembled monolayer-based hole-transporting layers (SAM-HTLs) that offer near-lossless contacts. They comprise a carbazole functional body with a phosphonic acid anchoring group.[7,28] Substantial differences in crystal growth of co-evaporated perovskites were observed, depending on whether or not MeO-2PACz was washed with ethanol to remove residual bulk SAM material before the deposition.[24] As the difference in contact angle for washed and unwashed MeO-2PACz is insignificant, as shown in our previous work,[29] the authors postulated that the difference in growth can be attributed to the formation of hydrogen bonds between exposed phosphonic acid functional groups and formamidinium iodide (FAI) during the deposition process. Hydrogen bonding between FA^+ cations and the substrate material has been extensively reported.[24,30,31] It has previously been attributed to a reduced formation energy for α-phase $FAPbI_3$,[24,30,31] as well as an increased defect formation energy and enhanced thermal stability, even for solution-processed perovskites.[30,32] Understanding of these interfacial mechanisms and their relation to evolving structural properties during perovskite crystal growth via co-evaporation is currently limited.

Recently, our group introduced deposition of nPACz SAM-HTLs of controlled thickness via thermal evaporation from a crucible in vacuum.[29] In the present work, we

[1] Light Technology Institute, Karlsruhe Institute of Technology (KIT), 76131 Karlsruhe, Germany

[2] Institute of Microstructure Technology, Karlsruhe Institute of Technology (KIT), 76344 Eggenstein-Leopoldshafen, Germany

[3] Heidelberg Institute for Theoretical Studies (HITS gGmbH), Heidelberg University, 69115 Heidelberg, Germany

[4] Interdisciplinary Center for Scientific Computing (IWR), Heidelberg University, 69115 Heidelberg, Germany

[5] Institute for Photon Science and Synchrotron Radiation (IPS), Karlsruhe Institute of Technology (KIT), 76344 Eggenstein-Leopoldshafen, Germany

[6] Institute for Chemical Technology and Polymer Chemistry (ITCP), Karlsruhe Institute of Technology (KIT), 76131 Karlsruhe, Germany

[7] Department of Chemistry and Biochemistry, University of Nevada, Las Vegas (UNLV), Las Vegas, NV 89154-4003, USA

[8] Department of Chemistry, University of Zürich, 8057 Zürich, Switzerland

[9] These authors contributed equally

[10] Lead contact

*Correspondence:
ganna.grynova@h-its.org (G.G.),
ulrich.paetzold@kit.edu (U.W.P.),
paul.fassl@kit.edu (P.F.)

https://doi.org/10.1016/j.matt.2024.02.004

Please cite this article in press as: Feeney et al., Understanding and exploiting interfacial interactions between phosphonic acid functional groups and co-evaporated perovskites, Matter (2024), https://doi.org/10.1016/j.matt.2024.02.004

employ a combination of this approach and standard solution-processed deposition of SAM-HTLs to perform an in-depth analysis of the impact of exposed phosphonic acid functional groups on co-evaporated perovskite film formation and whether it is mediated through interfacial hydrogen bonding. The presence of exposed phosphonic acid functional groups is controlled by washing the SAM layers with ethanol to remove unbound molecules. We demonstrate the immediate effect of the surface-dependent growth by comparing the maximum possible PCE of our co-evaporated PSCs on hydrogen bonding (non-washed) substrates with their non-bonding (washed) equivalents. Bulk properties and interfacial losses are explored via a combination of PV parameter analysis, X-ray diffraction (XRD), and photoluminescence quantum yield (PLQY) measurements. Critically, the presence of phosphonic acid functional groups has a substantial impact on the incorporation rate of organic cations, which strongly shifts the required FAI evaporation rate for optimal device performance. The presence of phosphonic acid functional groups appears beneficial for crystal growth, as it results in a preference for columnar crystal growth and effectively suppresses the formation of the photoinactive δ-FAPbI$_3$ phase during co-evaporation, which enables reproducible room-temperature formation of α-FAPbI$_3$.

We explore the hydrogen bonding between various organic cation materials and common SAM-HTLs via solution-based nuclear magnetic resonance (NMR). Furthermore, density functional theory (DFT) analysis of various SAM/perovskite combinations allows us to identify the chemical and physical causes for our observations. We find hydrogen bonding between surface iodine of the FAPbI$_3$ layer and phosphonic acid functional groups of nPACz that are of equal strength for α-FAPbI$_3$ and δ-FAPbI$_3$, indicating that such bonds are not directly responsible for the observed change in preferential growth to the α phase. Instead, we postulate a form of kinetic trapping whereby hydrogen bonding provides an energetic barrier for the conversion of α-FAPbI$_3$ to δ-FAPbI$_3$. We experimentally support this hypothesis through X-ray emission spectroscopy (XES) and XRD measurements of thin co-evaporated perovskite and FAI films grown on 2PACz ([2-(9H-carbazol-9-yl)ethyl] phosphonic acid) SAM-HTLs with and without exposed phosphonic acid functional groups.

This work elucidates the substrate impact on co-evaporated perovskite crystal formation and provides an explanation for how substrate-based phosphonic acid interactions lead to changes in organic incorporation rate and crystalline-phase formation due to the presence of hydrogen-bonding groups. In view of the need to develop reproducible and scalable fabrication methods, these results have important implications for future choices of substrate materials in evaporated perovskite-based single-junction and tandem devices.

RESULTS AND DISCUSSION

Performance comparison of evaporated and solution-processed nPACz layers

Typically, 2PACz and MeO-2PACz are integrated into p-i-n PSCs by solution-based methods.[7,33] Only recently, Farag et al. reported on the deposition of nPACz SAM-HTLs via thermal evaporation from a crucible in vacuum.[29] However, the above-discussed substrate influence on perovskite film formation makes their incorporation into all-evaporated PSC device stacks non-trivial. To evaluate the impact of SAM-HTLs with exposed phosphonic acids in co-evaporated p-i-n PSCs, we start by comparing maximum achievable device performances employing various 2PACz layers. Since differences have been previously observed for ethanol-washed and unwashed spin-coated MeO-2PACz layers,[24] we directly compare (1) evaporated unwashed, (2) evaporated washed, (3) spin-coated unwashed, and (4) spin-coated washed SAM-HTLs, as seen in Figure S1. In this comparison, we employ a double-cation perovskite absorber with the composition $Cs_{0.13}FA_{0.87}Pb(I_{0.95}Cl_{0.05})_3$ in the inverted p-i-n architecture: glass/indium tin oxide (ITO)/SAM-HTL/perovskite/C_{60}/SnO_x/Au. This composition is based on work by Lohmann et al., who performed bulk passivation of co-evaporated perovskites by incorporation of $PbCl_2$ employing four deposition sources.[34] To achieve the best PCE, the relative evaporation rate of FAI was optimized for each of the above SAM-HTL variations. More details can be found in the experimental procedures.

All solution-processed SAM-HTLs utilized high concentrations to guarantee a bulk component,[24] while evaporated SAM-HTLs featured a thickness of 4 nm, measured by a quartz-crystal microbalance (QCM). As unbound 2PACz has an approximate molecular length of 1.3 nm, it is expected that evaporated nPACz SAM-HTL layers with a thickness greater than a single molecule will exhibit a bulk component composed of unbound nPACz with exposed phosphonic acid functional groups. We expect a similar (but less controlled) bulk component in the case of solution-processed unwashed SAM-HTL layers. Bulk nPACz molecules are bound to the monolayer by van der Waals forces. π-π interactions between carbazole functional groups are particularly strong non-covalent bonds, which are expected to lead to the formation of a self-assembled bilayer with exposed phosphonic acid functional groups.[35] The strength of these interactions is dependent on substituents, and, hence, the density of exposed phosphonic functional groups may differ between various nPACz molecules.[36],[37] We note that this disordered bulk SAM layer is removed in part or even fully during standard solution-processed perovskite deposition, as observed in our previous work, where an extra washing step for a 6-nm-thick evaporated 2PACz film before perovskite deposition did not meaningfully impact PV parameters or PLQY compared to an unwashed film.[29] Furthermore, increasing the evaporated 2PACz thickness above that of the highest PCE (i.e., from 6 nm to 20 nm) yielded only minor changes in PLQY when solution-processed perovskite layers were deposited on top. However, evaporated perovskites do not disturb this bulk SAM layer, preserving exposed phosphonic acid functional groups. Therefore, the unwashed SAM-HTL layers are expected to impact device performance and perovskite film formation. A schematic is shown in Figure 1A for perovskite films grown on "bulk" and "monolayer" 2PACz, respectively. Hereafter, we refer to unwashed SAM layers with the presence of exposed phosphonic acids as bulk films and to washed SAM layers without exposed phosphonic acids as monolayer films.

Figures 1B and 1C provide current density-voltage (*J-V*) curves of the best-performing devices with each 2PACz variant. PSCs with monolayer solution-processed 2PACz achieve a maximum PCE of 17.0% with a fill factor (FF) of 0.77, an open-circuit voltage (V_{OC}) of 1.069 V, and a short-circuit current density (J_{SC}) of 20.6 mA cm^{-2} in the reverse scan direction, while PSCs with monolayer evaporated 2PACz achieve a comparable PCE of 16.7%, FF of 0.74, V_{OC} of 1.064 V, and J_{SC} of 21.4 mA cm^{-2}. PSCs with bulk films gave PV parameters of PCE 16.2%, FF 0.70, V_{OC} 1.074 V, and J_{SC} 21.5 mA cm^{-2} for solution-processed 2PACz, and PCE 16.0%, FF 0.69, V_{OC} 1.065 V, and J_{SC} 21.8 mA cm^{-2} for evaporated 2PACz, respectively. Full statistics, external quantum efficiency (EQE), reflectance, dark *J-V*, and maximum power point (MPP) measurements are provided in the supplemental information, along with datasets for optimized PSCs using MeO-2PACz and Me-4PACz ([4-(3,6-dimethyl-9*H*-carbazol-9-yl)butyl]phosphonic acid) as a SAM-HTL (Figures S3 and S4). The integrated J_{SC} values derived from EQE show currents of 20.2 mA cm^{-2} and 20.7 mA cm^{-2} for monolayer and 21.6 mA cm^{-2} and 22.1 mA cm^{-2} for bulk 2PACz from evaporated

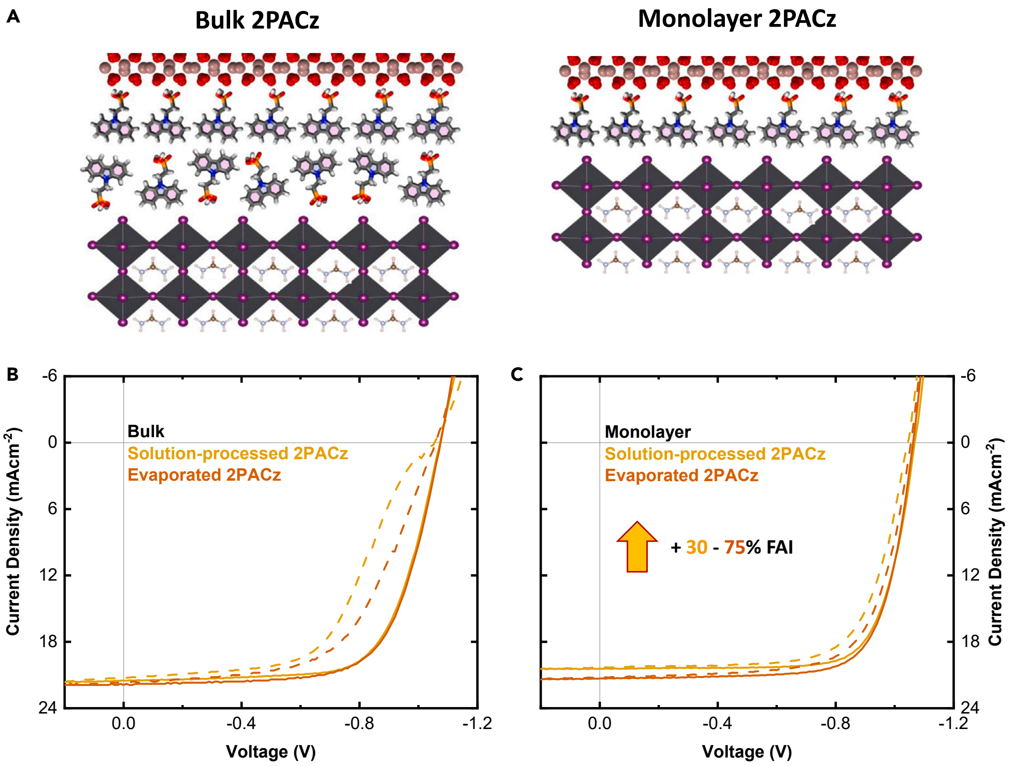

Figure 1. Visualizations of potential SAM/perovskite interactions and resultant *J-V* curves of best-performing PSCs

(A) Schematic of co-evaporated perovskite grown on bulk (left) and monolayer (right) 2PACz.

(B and C) *J-V* curves of the best-performing PSCs in reverse (solid) and forward (dashed) scan direction with evaporated (orange) and solution-processed (yellow) 2PACz: bulk SAMs (B) and monolayer SAMs (C), including a rough estimate of the required difference in FAI rate (+30% for solution-processed and +75% for evaporated 2PACz, respectively) to achieve maximum PCE.

and solution-processed sources, respectively. These values are within 10% of the *J-V* scan values, which is considered reasonably accurate.[38] Minor differences between J_{SC} from EQE and *J-V* are expected to be due to differences in measuring conditions. Notably, both monolayer and bulk evaporated 2PACz yield comparable maximum device performance in the reverse scan direction as compared to their solution-processed counterparts, reinforcing the suitability of evaporated 2PACz as an HTL for all-evaporated PSCs. PSCs with bulk films exhibit greater overall differences in PV parameters between evaporated and solution-processed nPACz, which we attribute to variations in the SAM layer thickness considering the lack of accurate methods to determine the thickness of ultrathin solution-processed layers or potential differences in the coverage and orientation of the bulk component. We assume comparable monolayer nPACz surface coverage on ITO between deposition methods due to the similar device performance and interfacial properties as also observed in our previous work.[29] However, we have no method of determining whether the bulk component coverage is also as comparable between evaporated and solution-processed layers. We note that the PCE at MPP of the best PSCs with bulk films is ~1.5%–2% absolute lower as compared to monolayer films (Figure S3), which could be attributed to a higher series resistance and possibly an enhanced magnitude of ion migration, in line with the observed significantly larger hysteresis in these samples.[39,40]

To understand potential interfacial differences for optimized co-evaporated perovskites on SAM-HTLs with and without exposed phosphonic acids, we examined the quality of the HTL/perovskite interface for the different 2PACz layers through an analysis series on the half-stack ITO/2PACz/perovskite. We refrain from introducing an electron transport layer (ETL) to exclude the known substantial non-radiative recombination losses at the perovskite/ETL interface when employing C_{60}.[41] For ideal bulk evaporated and solution-processed 2PACz, we obtain average implied V_{OC} values of 1.088 V and 1.045 V, respectively, compared to monolayer counterparts of 1.042 V and 1.052 V (Figure S5; respective PLQY data are shown in Figure S6). This indicates a slight change in surface recombination properties that persists independently of the deposition method. We note that the PLQY measurements are performed in ambient atmosphere, potentially explaining the slightly lower implied V_{OC} values as compared to the champion PSCs shown in Figure 1. The overall comparison of bulk against monolayer MeO-2PACz and Me-4PACz shows trends of increased implied V_{OC} for bulk SAM-HTLs (Figure S5). Ideality factors for optimized monolayer evaporated and solution-processed 2PACz are 1.46 and 1.45, respectively, while the bulk ideality factors are both 1.47 (Figure S7). This indicates no significant change in the recombination mechanism at the HTL/perovskite interface when comparing bulk and monolayer SAM-HTLs.

We employed time-correlated single-photon counting (TCSPC) measurements to determine charge-carrier lifetimes. The decays are typically fitted with either a biexponential, a triexponential, or even a stretched exponential function, with a relatively high weighting of non-radiative Shockley-Read-Hall (SRH) lifetimes,[42] which makes decay lifetimes difficult to compare.[43] The typically observed fast initial decay is associated with monomolecular non-radiative trapping-detrapping processes, interfacial recombination, and charge-transfer processes into the contact layers.[43,44] While analysis of solution-processed perovskites can exclude charge transport layers to minimize these effects, substrate-dependent growth of co-evaporated perovskites prevent such experiments.[23] Therefore, our discussion will focus on lifetimes obtained from a monoexponential fit of a truncated region of decay data at later times measured at low excitation fluence (initial charge-carrier density of $\sim 3 \times 10^{14}$ cm^{-1}) (Figure S8 and Table S1).[32,41,43] These lifetimes we correlate to SRH recombination both in the bulk of the perovskite and at the SAM-HTL/perovskite interface, allowing us to compare the optoelectronic quality of the various half-stacks. Lifetimes obtained from a biexponential fit are also provided in Table S1 as comparison. We observe similar SRH lifetimes for monolayer evaporated and solution-processed 2PACz, with averages of 277.6 ± 1.4 ns and 268.7 ± 1.5 ns, respectively. Notably, SRH lifetimes are much higher for bulk solution-processed SAMs, with 1,080.9 ± 10.3 ns in the case of 2PACz. We observe similar trends for MeO-2PACz and Me-4PACz. These results are in line with the previously discussed slightly higher implied V_{OC} values for bulk SAMs, indicating that a thicker SAM layer more efficiently suppresses non-radiative recombination at the HTL/perovskite interface.

While PSCs with monolayer SAMs unilaterally outperform that with bulk SAMs, the process of obtaining a nearly stoichiometric composition to achieve maximal PCE reveals a critical difference between each studied HTL. With constant inorganic evaporation rates, monolayer SAM-HTL layers require substantially higher FAI evaporation rates to obtain maximum PCE, with approximately 30% higher rates required for washed solution-processed layers and approximately 75% higher rates required for washed evaporated layers compared to the respective bulk counterpart (Figure 1C). We attribute a potential cause for this difference between deposition methods to different densities of phosphonic acids at the surface for bulk films. This could be due to the SAM layer thickness, or potentially indicates that evaporation allows more ready π-π interactions between carbazole functional groups and

Please cite this article in press as: Feeney et al., Understanding and exploiting interfacial interactions between phosphonic acid functional groups and co-evaporated perovskites, Matter (2024), https://doi.org/10.1016/j.matt.2024.02.004

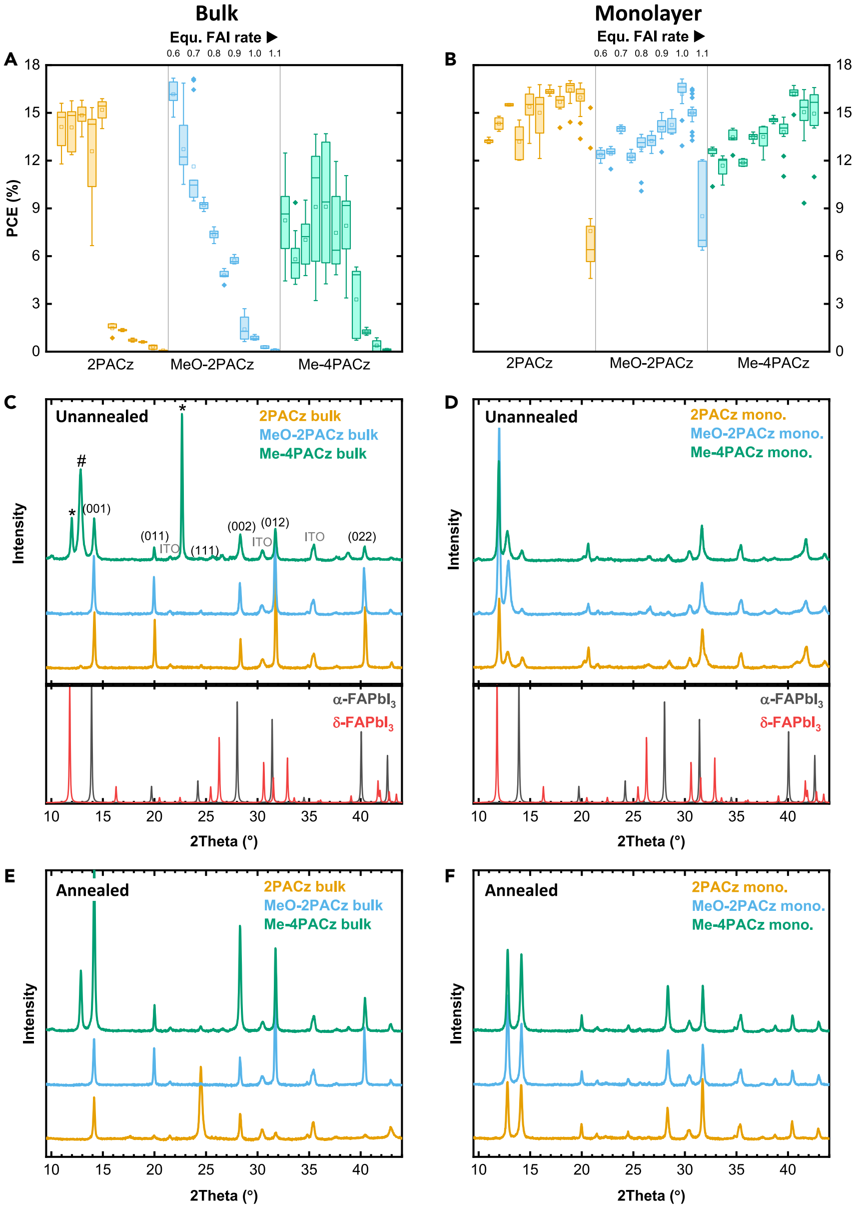

Figure 2. Device performance and crystal structure changes between materials and deposition methods

(A and B) Statistical trends of PCE for p-i-n PSCs with varying rates of FAI for solution-processed nPACz as SAM-HTLs, as deposited to leave residual bulk material (A) and with a washing step to form a monolayer (B). For each series, the equivalent FAI rate is varied from 0.6 Å s^{-1} to 1.1 Å s^{-1} in 0.05 Å s^{-1} steps. Only the reverse scan is shown. Sample number ranged from 4 to 16, with an average of 10 per condition. The only exception was 0.7 Å s^{-1} monolayer 2PACz, which has 3 samples. Relevant FF, J_{SC}, and V_{OC} are present in Figures S9 and S10.

(C–F) XRD of unannealed (C and D) and annealed (E and F) films, deposited at the same stoichiometry as the best-performing PSCs with bulk (C and E) and monolayer (D and F) solution-processed nPACz. In (C), δ-$FAPbI_3$ peak locations are labeled with an asterisk and PbI_2 peak locations with hash mark; ITO peaks and important perovskite orientations are given. Reference patterns from ICSD data for α-$FAPbI_3$ and δ-$FAPbI_3$ are also shown. We assign the Me-4PACz peak at 22.6° to δ-$FAPbI_3$; the overpronounced height is attributed to highly irregular surface coverage (see Figure S13).

hence a greater alignment in the bulk component. Optimal PSCs shown in Figure 1 correspond to equivalent FAI rates of 1.05 Å s^{-1} for monolayer solution-processed 2PACz, 1.05 Å s^{-1} for monolayer evaporated 2PACz, 0.8 Å s^{-1} for bulk solution-processed 2PACz, and 0.6 Å s^{-1} for bulk evaporated 2PACz (see experimental procedures for more details).

As comparison, we provide *J-V* curves of respective PSCs with monolayer 2PACz utilizing equivalent FAI rates optimized for bulk 2PACz in Figure S2, clearly demonstrating strong differences and decreased performance. Literature has previously established that, especially for co-evaporated perovskites, the initial growth conditions can strongly impact the bulk. This has been shown both for the crystal structure of the bulk material and for the organic incorporation rates.[20,23] We posit that a similar mechanism is occurring in this case. We note that cursory XRD and PLQY peak position analysis did not identify a shift in (001) peak position or PLQY wavelength with respect to bulk or monolayer component, which is interpreted to mean that composition is approximately comparable between samples. We cannot exclude the possibility that the observed change in required FAI rate would result in a different stoichiometry for compositions with different halide content (i.e., Br and/or Cl), but testing this was beyond the scope of the current work. These results potentially allow higher overall deposition rates for perovskite growth without impacting composition or resulting in thermal decomposition.[45]

Growth trends of perovskites on various nPACz substrate configurations

Expanding the trend observed for 2PACz to other nPACz materials (MeO-2PACz and Me-4PACz) reveals that all solution-processed bulk nPACz layers require approximately ∼23%–30% lower FAI rates to achieve maximum PCE compared to their monolayer counterparts, an extreme example of substrate-dependent growth. However, previous reports on substrate-dependent growth did not find substantial changes in the required process window,[23,24] while our findings show the need for large changes in rate even for chemically very similar substrate materials. To clearly demonstrate the large shifts in optimal FAI deposition rate, a stoichiometry series was undertaken for monolayer and bulk 2PACz deposited via spin coating. For a set perovskite composition, $Cs_{0.13}FA_{0.87}Pb(I_{0.95}Cl_{0.05})_3$, the equivalent FAI rate was varied to identify the optimal performance with respect to PV parameters, as shown in Figure 2. Samples were characterized with *J-V* measurements to determine trends in device performance, and XRD was performed on unannealed and annealed perovskite films that gave the highest PV performance to explore differences in crystal growth on various SAM-HTLs. Full statistics and a truncated series employing evaporated SAM-HTLs can be found in Figures S9–S12.

One clear observation is a rather sudden drop in PCE at a certain equivalent FAI rate, primarily induced by a substantive drop in J_{SC}, for most SAM-HTLs (Figures 2A and S9–S12). This is associated with excess organic cations in the perovskite film,[24,46,47] and the presence of this drop is therefore attributed to a change in the required FAI rate for ideal stoichiometry. This drop is specifically reached for all bulk SAMs, which exhibit a rather small processing window for high PCE, while for monolayer SAMs the processing window is larger and only the highest studied FAI rate shows a strong drop in PCE (e.g., for 2PACz and MeO-2PACz).

While our perovskite film takes the form $Cs_{0.13}FA_{0.87}Pb(I_{0.95}Cl_{0.05})_3$, in our discussion of observed crystal phases, for simplicity we refer to it as α-$FAPbI_3$ and δ-$FAPbI_3$, as the inclusion of Cs and Cl do not prevent the formation of phases analogous to pure FA perovskites. For sufficiently low Cs or Cl content, as in our perovskite, the

Please cite this article in press as: Feeney et al., Understanding and exploiting interfacial interactions between phosphonic acid functional groups and co-evaporated perovskites, Matter (2024), https://doi.org/10.1016/j.matt.2024.02.004

inclusion of such materials will, for example, lead to a minor shift in peak position (i.e., the (001) peak shifts from 13.98° to 14.08° for 10% Cs) but not to peak splitting or other meaningful changes.[48–50] Comparing peak positions of (001) peaks for PbI_2, α-$FAPbI_3$, and δ-$FAPbI_3$ does not reveal significant changes between samples. We observe a shift from an expected position from the Inorganic Crystal Structure Database (ICSD) $FAPbI_3$ reference of 13.9° to an average of 14.16° for the α phase and from 13.78° to 13.98° for the δ phase of our perovskite. We attribute these results to differences in measurement setup or the different stoichiometry of our samples compared to the $FAPbI_3$ reference.[48,50]

Comparing monolayer and bulk nPACz, the XRD patterns of glass/ITO/SAM-HTL/perovskite half-stacks displays three noteworthy changes. First, a strong prevalence of δ-$FAPbI_3$ XRD peaks (at 11.79°) was observed for unannealed perovskite films grown on monolayer nPACz films (Figure 2D), which is not present in unannealed films grown on bulk 2PACz and MeO-2PACz. The latter exclusively exhibit α-$FAPbI_3$ XRD peaks, indicating room-temperature formation of α-$FAPbI_3$. An exception to this trend is observed for Me-4PACz; however, this can readily be attributed to uneven film coverage, which has been previously observed for solution-processed Me-4PACz layers.[51–55] Poor wettability has been theorized to be caused by the formation of SAM micelles, which require lower concentrations of SAM materials with longer alkyl chains.[55] This is further indicated by the fact that perovskites co-evaporated on bulk solution-processed Me-4PACz display dot-like coverage that is not present in equivalent perovskites on bulk evaporated Me-4PACz (Figure S13), an effect that is reduced for washed monolayer Me-4PACz films. The second noteworthy XRD change is the significantly reduced presence of crystalline PbI_2 in annealed films in the case of bulk SAMs. The presence of significant PbI_2 peaks for monolayer films potentially indicates that perovskite film growth was non-ideal in terms of organic cation adsorption. Uneven coverage of Me-4PACz is a potential explanation for the continued presence of a PbI_2 peak in bulk layers of that material. Finally, significant changes in relative XRD peak intensity are observed that are related to changes in preferential growth.[23] First, perovskites grown on bulk nPACz materials exhibit a decreased relative intensity of the (001) crystal plane compared to secondary planes (Figure S14). Most notable ratios of peak areas compared to the (001) plane are 2.99 for the (111) plane of bulk 2PACz compared to 0.06 for the comparable monolayer, and 1.71 for the (012) plane of bulk MeO-2PACz compared to 0.56 for the comparable monolayer. In general, bulk nPACz displays significant variation in peak intensity and distribution between materials, presented in Figure S14.

As all SAM materials were deposited using equimolar solutions, we consider this a potential indicator that the density and arrangement of exposed phosphonic acid functional groups can differ between bulk materials. We propose two mechanisms to explain the differences in observed growth. The first relates exclusively to Me-4PACz, which exhibits uneven coverage that would lead to unexpected perovskite phases as large regions of the film are potentially covered by a monolayer or bare ITO, both of which significantly impact perovskite growth. As a more general mechanism, π-π interactions between carbazole functional groups are substituent dependent,[36,37] causing the expected density of ‘‘bilayer’’ nPACz materials with exposed phosphonic functional groups to differ between our materials. This is coupled with the expected orientation of phosphonic acid functional groups to become non-uniform at low coverages due to the potential for tilted SAM configurations,[28] which are more likely with increasing alkyl chain length. Changes in this density of exposed phosphonic acids may also explain the differences in relative FAI rate required for the highest-performing devices. Relative peak areas of monolayer

Please cite this article in press as: Feeney et al., Understanding and exploiting interfacial interactions between phosphonic acid functional groups and co-evaporated perovskites, Matter (2024), https://doi.org/10.1016/j.matt.2024.02.004

nPACz are roughly comparable for the studied peaks, indicating approximately comparable growth (Figure S14). A high degree of similarity also indicates that the additional functional groups present on exposed carbazole for monolayer conditions do not significantly impact FAI optimal rate or perovskite growth. The comparable optimal FAI rates for monolayers also indicate that similar coverage of the ITO is expected.

Previous work has attributed both minimization of a residual crystalline PbI_2 signal and increases in the peak intensity of crystal planes other than (001) as signifiers of a more suitable substrate for co-evaporation.[23] Specifically, they postulate that a change in relative peak intensities to favor (011), (111), and (012) compared to (001) as indicative of columnar growth.[23,24] To shed light on this, we performed cross-sectional and surface scanning electron microscopy (SEM) of completed devices with perovskite grown on bulk and monolayer 2PACz. Visual differences in grain orientation are not as self-evident as in our previous work[23] although we still observe a slight tendency for a reduced number of vertical grain boundaries potentially indicative of more columnar growth (Figure S15). Average crystal grain sizes, determined from surface SEM measurements, do not show significant differences between underlayers (113.7 ± 4.73 nm for bulk and 100 ± 3.2 nm for monolayer 2PACz). However, we observe some grains with a significantly higher SEM response for the monolayer sample, leading to brighter coloration, which have previously been associated with Pb-rich perovskite grains,[33] supporting the increased PbI_2 observed in the corresponding XRD.

To corroborate that the observed XRD changes stem from the discussed differences between monolayer and bulk SAMs prompted us to form a monolayer film with exposed phosphonic acids. Al-Ashouri et al. recently showed that incorporating 1,6-hexylenediphosphonic acid (6dPA) into Me-4PACz results in SAMs with exposed phosphonic acid functional groups.[53] As the present work primarily focuses on 2PACz, we replicated this effect with 1,4-butylenediphosphonic acid (4dPA). For this, washed 2PACz/4dPA films with varying molar fractions (0%, 10%, 20%, 30%, 60%) of 4dPA were prepared. Perovskites were deposited at 0.75 $\text{Å}\ s^{-1}$ equivalent FAI rate, which is expected, in the presence of exposed phosphonic acids, to form exclusively α-$FAPbI_3$ during co-evaporation (i.e., for unannealed perovskite films). Indeed, as shown in Figure S16, increasing the molar fraction of 4dPA directly correlates with a trend of decreasing intensity in the (001) δ-$FAPbI_3$ XRD peak and increasing intensity of the (001) α-$FAPbI_3$ XRD peak, with complete conversion observed for 60% 4dPA, confirming our expectations.

Inclusion of 4dPA into devices at all tested molar fractions resulted in reduced PCE compared to bulk or monolayer SAMs with equivalent FAI rates (Figure S17). Due to the impact of excess PbI_2 on PV parameters,[47,56] comparisons of said parameters between samples are inherently not reliable, as an increase in 4dPA leads to a decrease in excess PbI_2 (Figure S16), probably due to increased incorporation of organic cations. The maximum V_{OC} remains steady up to 20% 4dPA, while average V_{OC} decreases slightly, before a sharp decline at 30% and above. A potential explanation is increased FAI absorption due to the high density of exposed phosphonic acids leading to an excess. However, excess FAI causes a non-linear drop in V_{OC} (compare Figure S9) as opposed to the linear decrease observed with respect to 4dPA concentration. We attribute the V_{OC} drop (and related lower PCE compared to bulk or monolayer 2PACz) to the insulating behavior of alkyl linkers, with any inclusion of 4dPA reducing the conductivity and hole-extraction capabilities of 2PACz.

Please cite this article in press as: Feeney et al., Understanding and exploiting interfacial interactions between phosphonic acid functional groups and co-evaporated perovskites, Matter (2024), https://doi.org/10.1016/j.matt.2024.02.004

Abzieher et al. estimated surface polarity via contact angle measurements with an H_2O droplet, which was correlated with preferential crystal growth during co-evaporation.[23] In our case, however, washed and unwashed 2PACz and MeO-2PACz substrates deposited via evaporation or spin coating displayed no consistent difference in contact angle for any of the studied materials (Figure S18), excluding it as an explanation for the observed differences in the required relative organic cation rate. Therefore, we conclude that the presence of exposed phosphonic acid functional groups has a greater impact on interfacial interactions and determining perovskite growth than surface polarity. Combined, these results support the presence of an interaction between exposed phosphonic acid functional groups and the perovskite during film formation. These exposed groups are not present in the case of monolayer nPACz films but are highly likely in bulk materials.[35] This can explain the observed differences between unwashed evaporated and solution-processed films, as the effect appears dependent on the density of phosphonic acid functional groups and was previously attributed to hydrogen bonding to FA^+ cations.[24] However, the significant impact on perovskite film formation and PV parameters prompts an in-depth investigation of this process, which will be conducted in the following sections.

Presence and strength of hydrogen bonding between phosphonic acid functional groups and organic cations studied by liquid-phase NMR analysis

Previous literature indicates two dominant forms of hydrogen bonding between phosphonic acid functional groups and FAI,[24,32,57] (1) H…O hydrogen bonding between the phosphonic acid and amidine moiety from the FA^+ and (2) OH…I hydrogen bonding between the phosphonic acid and iodine. To better understand the specific form of this interaction for nPACz materials, a series of liquid-state ^1H NMR measurements was conducted. Reference raw spectra of 2PACz and FAI dissolved in a deuterated dimethylsulfoxide (DMSO) solvent are shown in Figure 3A. Upon the introduction of equimolar 2PACz to the FAI solution, a number of notable changes can be observed in the FAI spectra as shown in Figure 3B. Protons attributed to the amidine moiety split into two doublets. This splitting is attributed to the hindered rotation of FA^+ amidine groups caused by the formation of a delocalized double bond planarizing the molecule, disrupting the equivalent chemical environment between amidine protons.[58] Interactions with the CH proton occur through vicinal 3J *cis* and *trans* coupling (coupling constant J_{trans} = 15.2 Hz). Furthermore, the CH protons split into a triplet of a triplet (tt) (coupling constants J_{cis} = 6.4 Hz and J_{trans} = 15.1 Hz) due to interaction with the inequivalent amidine protons. Splitting of such NMR signals is described in the literature but its origin remains unclear, with some publications attributing it to the introduction of a Lewis acid.[59] Concurrent changes can be found within the 2PACz spectra by comparison with the reference peak for the phosphonic acid functional group at 8.80 ppm (compare Figure 3A). Here, a clear chemical shift is observed; upon introduction of FAI, the peak shifts to 6.68 ppm for a 0.5 M ratio of 2PACz to FAI, while it increases to 9.67 ppm with increasing 2PACz concentration as shown in Figure 3C.

To determine which form of hydrogen bonding is present and to derive a material-dependent trend for bonding strength, several liquid-phase series were conducted. These series investigate interactions between common organic perovskite cations (methylammonium iodide [MAI], FAI, guanidinium iodide [GAI]), with 2PACz as a constant SAM-HTL, as shown in Figure 3D. A second series comparing interactions between FAI and two phosphonic acid-containing SAM-HTLs (2PACz and MeO-2PACz) is shown in Figures S19 and S20, along with all NMR spectra. Measurements with Me-4PACz were attempted, but due to peak broadening and a relatively low

Please cite this article in press as: Feeney et al., Understanding and exploiting interfacial interactions between phosphonic acid functional groups and co-evaporated perovskites, Matter (2024), https://doi.org/10.1016/j.matt.2024.02.004

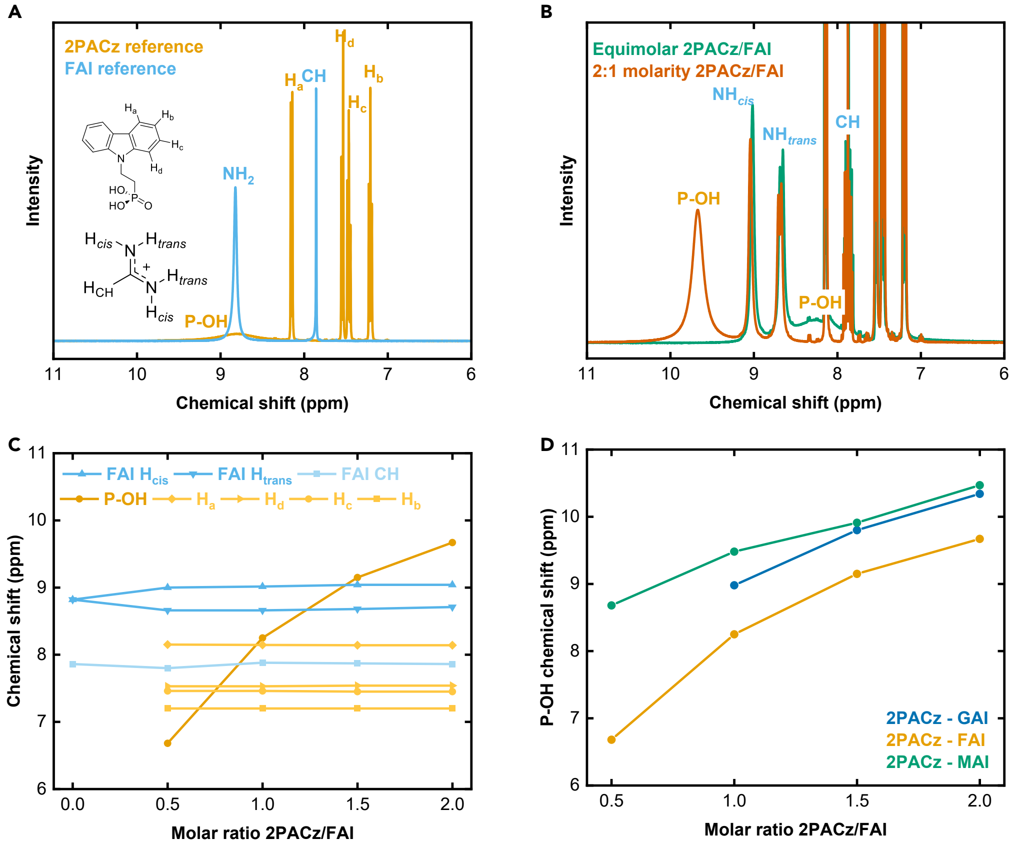

Figure 3. NMR series identifying the form of hydrogen bonding

(A) Solution-NMR of pure FAI and pure 2PACz solutions. The inset illustrates the *cis* and *trans* variation of the deplanarized FA^+ molecule.

(B) Solution-NMR of FAI solution with two concentrations of 2PACz.

(C) Trend of chemical shift for each signal as a function of 2PACz concentration, indicating no shift in FAI NMR peak locations with increasing 2PACz concentration.

(D) Chemical shift trends of P-OH peak for GAI, FAI, and MAI with varying concentration of 2PACz. Relevant NMR spectra corresponding to the stated shifts are shown in Figure S19.

peak intensity, the potential error in determining the peak position is too substantial for meaningful analysis; thus, the trend of phosphonic acid peak shift of Me-4PACz series was excluded from our analysis (raw spectra are shown in Figure S21). Organic cation concentrations were maintained at 0.13 M, while 2PACz concentration was varied from 0 M to 0.26 M. A slight shift of the phosphonic acid signal of 2PACz was observed when changing the concentration in the absence of a halide source. This is attributed to interactions of phosphonic acids in non-polar and aprotic solvents such as d6-DMSO, which was employed for this study.[60] Despite a clear shift in the phosphonic acid with respect to material concentration, there is no complementary shift in the organic cation peak positions, as is evident in Figure 3C. Furthermore, peak shift magnitudes are roughly equivalent between organic cations (Figure 3D). This indicates that hydrogen bonding between the organic portion of these materials and the phosphonic acid functional groups is not observed in solution. An alternative explanation, rendered much more likely due to the equivalent shift for each cation, would be the formation of a hydrogen bond between the halide portion of these materials and the phosphonic acid.[61] This indicates that the observed interactions and, hence, changes in optimal organic cation rate and crystallization, are potentially not exclusive to FAI. Furthermore, varying 2PACz/PbI_2 results in comparable peak shifts (Figure S22), indicating that such interactions are not

Please cite this article in press as: Feeney et al., Understanding and exploiting interfacial interactions between phosphonic acid functional groups and co-evaporated perovskites, Matter (2024), https://doi.org/10.1016/j.matt.2024.02.004

exclusive to organic precursors. However, the direct deposition nature and reduced substrate dependence of inorganic precursors[23,45,62] means we do not expect such interactions to meaningfully impact growth.

It is important to note that materials capable of hydrogen bonding in inert solvents are naturally expected to shift peak positions with changing concentration, as demonstrated in Figure S23.[60] Furthermore, the peak position for reference 2PACz (8.80 ppm) being inconsistent with the broader 2PACz/FAI trend in Figures 3C and 3D indicates that this system is more complex than the pure 2PACz case, which we rationalize as indicative of non-comparable interaction mechanisms. Hence, we cannot precisely quantify the strength of potential hydrogen bonding between phosphonic acid functional groups and halides of organic cation precursors, and our liquid-phase results are considered qualitative rather than quantitative. However, this does not invalidate our observation that hydrogen bonding is not observed between phosphonic acid and the organic portion of these organic cation precursors. Our repeated study using MeO-2PACz and Me-4PACz (Figures S20 and S21) supports this hypothesis and indicates that the hydrogen-bonding strength is approximately equivalent between nPACz materials. Any further interactions of MeO-2PACz through the methoxy groups were excluded, as no significant shifts of the corresponding signal were observed. Consequently, in all cases, intermolecular interactions primarily stem from hydrogen bonding of free phosphonic acid functional groups with present halide ions.

Understanding interactions between phosphonic acid functional groups and perovskites

To gain atomistic-level insights into the interaction mode of phosphonic acid functional groups with evaporated perovskites and to understand whether these interactions can form the basis for the experimentally observed crystal growth rate and orientation differences between each substrate, we modeled these systems using DFT. We utilized PBE-D3, which is considered highly accurate for numerous modeling applications,[63,64] including perovskites.[65] $FAPbI_3$ was chosen as a simplified perovskite model (as FA^+ is the dominant cation in the investigated perovskite), with 2PACz as the SAM-HTL. Additional functional groups or variations in alkyl chain length are not expected to significantly impact the studied interactions and were thus not included in our *in silico* models. Our DFT calculations consider two potential $FAPbI_3$ unit cells, the photoinactive hexagonal phase (δ-$FAPbI_3$) and the photoactive cubic phase (α-$FAPbI_3$). Secondary photoactive phases, the orthorhombic β-$FAPbI_3$ and tetragonal γ-$FAPbI_3$ to be precise, were not investigated, as their formation requires temperatures below 153 K and 93 K, respectively, which were deemed too extreme for standard perovskite film formation.[61]

The role of FA^+ cation orientation in the stability of α-$FAPbI_3$ and δ-$FAPbI_3$ perovskites is well established in literature.[61,66,67] Free rotation of the FA^+ cation within α-$FAPbI_3$ increases the entropy of this phase as temperature rises, making it the most stable phase at temperatures above ~430 K.[67] δ-$FAPbI_3$ is more stable at room temperature, due to its large unit cell and, thus, lower energetic cost of encapsulating the large FA^+ cation. The position of the latter is fixed within the δ-$FAPbI_3$ via C…I and NH_2…I interactions, and hence the associated entropic gain is insignificant compared to the α-phase.[68] The position of the FA^+ cation within the cubic and hexagonal phases were optimized using DFT at the PBE level (see experimental procedures for computational details). Similar to the findings of Zheng et al.,[67] free FA^+ ions position themselves in the midplane of the α-$FAPbI_3$ unit cell, oriented along the plane to minimize C…I and NH_2…I contacts. Conversely, for δ-$FAPbI_3$ a complex

Please cite this article in press as: Feeney et al., Understanding and exploiting interfacial interactions between phosphonic acid functional groups and co-evaporated perovskites, Matter (2024), https://doi.org/10.1016/j.matt.2024.02.004

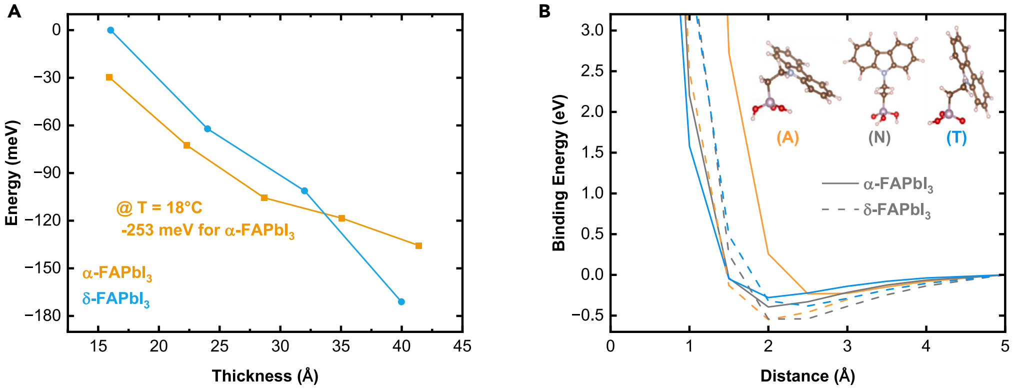

Figure 4. DFT results of thin perovskite slabs with and without interaction energies between 2PACz and thin perovskite slabs

(A) Stability of α-FAPbI$_3$ and δ-FAPbI$_3$ slabs, determined by energy per unit cell as a function of slab thickness. These values do not include entropic contribution or surface functionalization.

(B) Binding energy of various 2PACz conformations as a function of the distance between substrate and material for both phases of FA$^+$-terminated FAPbI$_3$ perovskite. Inset: investigated 2PACz conformations. In these simulations, phosphonic acid is assumed to be directly exposed to the perovskite surface, corresponding to a bulk film.

arrangement is formed, featuring ribbons of coordinated PbI$_3$ and interstitial FA$^+$ with fixed orientations between parallel ribbons to minimize C…I and NH$_2$…I contacts. Encapsulation of FA$^+$ cations lowers unit cell strain, resulting in a free energy difference of 279 meV under bulk conditions. A visualization of these geometries and the associated interaction modes is present in Figure S24.

We next simulated a perovskite slab with thickness below 50 Å in the absence of any surface interactions to allow the structures to fully relax. Due to the variation in unit cell size between α-FAPbI$_3$ and δ-FAPbI$_3$, interpolation was required for intermediary thicknesses. Critically, in the absence of entropic contributions for equivalent slab thicknesses, α-FAPbI$_3$ is more stable than δ-FAPbI$_3$ in the region below 35 Å, with an energy difference of 30 meV at the lowest simulated thickness of ~16 Å (Figure 4A). The reason for this unexpected stability is the fact that the surface energy is lower in α-FAPbI$_3$ (compared to δ-FAPbI$_3$) in the thin slab limit. Entropic contributions will further favor α-FAPbI$_3$ due to the free movement of interstitial FA$^+$, which is restricted in δ-FAPbI$_3$. These effects, estimated as ~−253 meV at 18°C, make α-FAPbI$_3$ more stable at the early stage of the growth and increase the thickness at which we approach the bulk condition of thermodynamically favored δ-FAPbI$_3$. These results can explain the existence of a small α-FAPbI$_3$ peak in the XRD of unannealed co-evaporated perovskite thick films grown on monolayer SAM-HTLs (Figure 2D).

Theoretical results so far suggest that the α phase is favored at the early stages of the crystal growth, yet δ-FAPbI$_3$ is thermodynamically preferred in the bulk limit. Given that α-FAPbI$_3$ is the only crystalline phase observed experimentally in unannealed perovskite films deposited on bulk nPACz (except for Me-4PACz), we next tested the possibility that the presence of phosphonic acid promotes α-FAPbI$_3$ growth over δ-FAPbI$_3$. For three configurations of the 2PACz molecule (A, anionic; N, neutral; and T, *trans* conformation), computed binding energies with FA$^+$- and Pb-terminated perovskite α-FAPbI$_3$ and δ-FAPbI$_3$ were found to be relatively similar for the two phases (Figure 4B), with the strongest interactions occurring at distances of ~2 Å, commensurate with non-covalent interactions (NCIs) (such as hydrogen bonding) rather than covalent bonds. The interaction profile for a Pb-terminated perovskite was also considered and is presented in Figure S25. Computed NCI

Please cite this article in press as: Feeney et al., Understanding and exploiting interfacial interactions between phosphonic acid functional groups and co-evaporated perovskites, Matter (2024), https://doi.org/10.1016/j.matt.2024.02.004

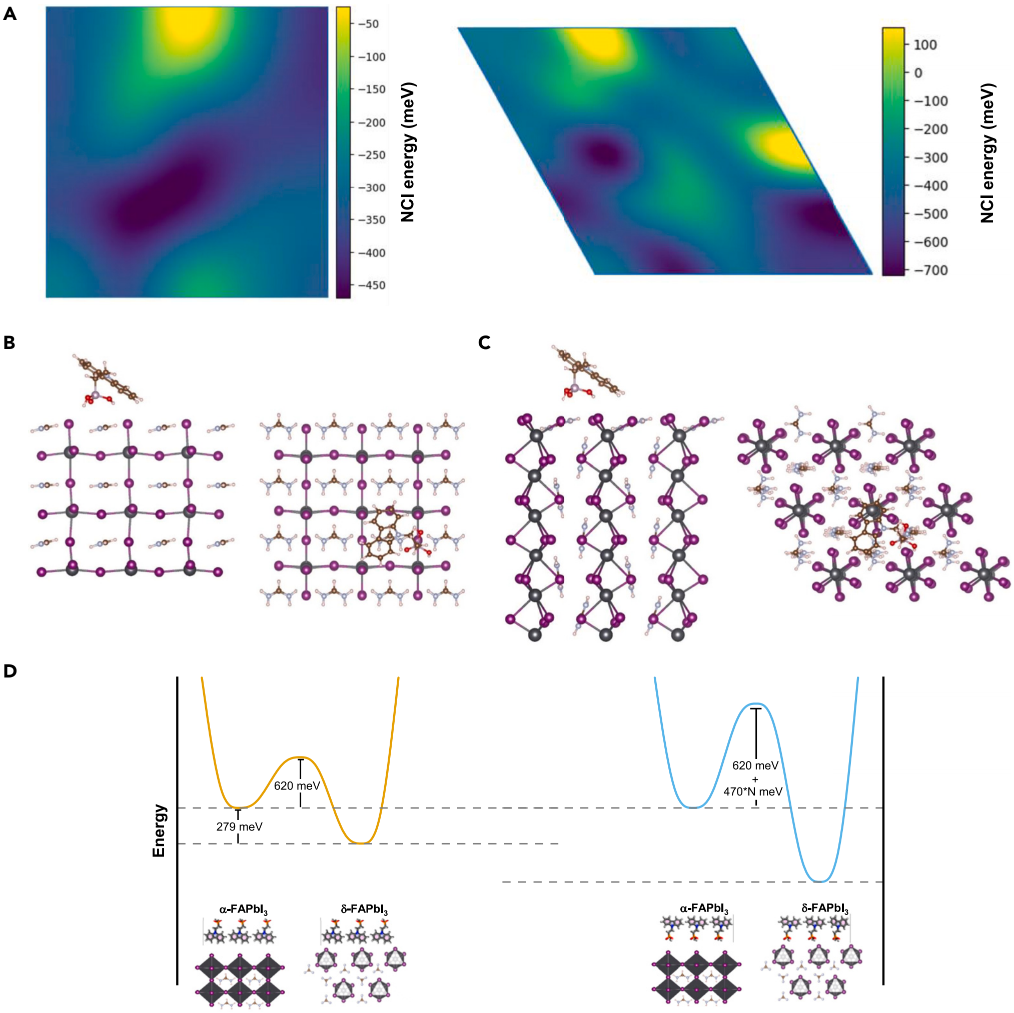

Figure 5. DFT visualizations of interactions between nPACz and perovskites, with explanations for how such changes apply to bulk materials

(A) Computed non-covalent interaction (NCI) energies for laterally shifted 2PACz, fixed at a 2 Å distance from the surface of α-FAPbI$_3$ (left) and δ-FAPbI$_3$ (right).

(B and C) Geometries corresponding to the NCI energy minima of 2PACz on α-FAPbI$_3$ (B) and δ-FAPbI$_3$ (C) surfaces (side and top views).

(D) Energy diagram representation of kinetic trapping for α-FAPbI$_3$ stabilization. Activation energy of phase transitions in the absence of phosphonic acid functional groups was taken from Chen et al.[69]

energies were essentially unchanged for each perovskite phase, and we observe comparable interaction strength between the 2PACz and the perovskite surface for both FA$^+$- and Pb-terminated slabs. All associated data points for these plots are presented in Tables S2–S4.

To better capture the diverse interaction modes between 2PACz and perovskite, we scanned interaction energy profiles by laterally shifting the 2PACz molecule at a fixed 2 Å distance above the 3 × 3 (001) perovskite surface (Figure 5A). Maximum computed energies of 470 meV for α-FAPbI$_3$ and 720 meV for δ-FAPbI$_3$ suggest that interactions with the phosphonic acid alone cannot explain the experimentally observed preference for the α phase. Geometries corresponding to the minima of the scanned interaction energies, shown in Figures 5B and 5C, reveal shortened contacts between the OH group of the phosphonic acid in 2PACz and surface iodine anions of the perovskite. This finding is in good agreement with our liquid-phase NMR observations, which indicate that bonding primarily occurs between phosphonic acid functional groups and the halide component of organic cations, supporting the notion that such interactions are not exclusive to FA-based perovskites. These findings also provide further evidence that halide interactions are more relevant for this interface than other potential interactions such as FA^+ or Pb^{2+}.

Our results indicate that, while α-$FAPbI_3$ is thermodynamically preferred at the initial stages of film formation, δ-$FAPbI_3$ is both the dominant phase in the bulk limit and the phase more strongly stabilized by interactions with the phosphonic acid moieties of 2PACz. We therefore put forward the following mechanism explaining the experimentally observed preference for the α-$FAPbI_3$, based on the concepts of kinetic and chemical trapping (Figure 5D). Specifically, α-$FAPbI_3$ is formed initially and preferentially to δ-$FAPbI_3$ due to kinetic (entropic) contributions outlined in Figure 4A, combined with the lowering of the surface energy outlined in Figure 5A.[66,69] Interaction with free phosphonic acid moieties introduces a passivation barrier for the conversion of α-$FAPbI_3$ to δ-$FAPbI_3$ when transitioning from thin film to bulk limit, i.e., a kind of "chemical trapping." According to Chen et al.,[66,69] cubic (α-$FAPbI_3$) and hexagonal (δ-$FAPbI_3$) space groups lack a simple group/subgroup connection. Transitioning from a cubic to a hexagonal phase involves complex movements and Pb–I bond breaking and forming. Therefore, such a phase transition first requires dissociation of the perovskite film from the 2PACz molecules. The height of the corresponding passivation barrier is equivalent to N*470 meV, where N is the maximum number of phosphonic acid functional groups per 3 × 3 (001) surface (Figure 5D). Interfacial passivation strategies have been previously shown to enhance the stability of α-$FAPbI_3$ and to reduce the formation of δ-$FAPbI_3$ through similar surface functionalization and entropic stabilization.[68] Critically, co-evaporated perovskites grow at a relatively low rate compared to solution-processed or sequentially evaporated films, making them more vulnerable to this trapping effect.

To obtain a better experimental understanding of this process and investigate the impact of interactions at the interface between the SAM-HTL and the perovskite film, synchrotron-based soft XES was employed to determine the element-specific electronic structure at the nitrogen atoms. For this purpose, we measured non-resonant N K XES spectra ($h\nu$ = 420 eV) of two different sample sets: bulk evaporated 2PACz and monolayer evaporated 2PACz. On each substrate, a ~25-nm FAI or ~25-nm perovskite film was deposited, similar to our previous work on FA-based perovskites.[70] We chose evaporation as a deposition method due to the high degree of substrate uniformity. For the bulk 2PACz substrate, we also measured the interface formation with ~25 nm PbI_2 and ~25 nm CsI. Additionally, the ITO substrate, a 2PACz bulk powder reference, and a bulk $FAPbI_3$ were measured, while the reference FAI spectrum was used from previous work.[71]

The ITO N K XES spectrum (Figure 6A, bottom) exhibits a broad (and relatively weak) spectral structure with a main peak at ~394 eV. While not necessarily expected in an ITO film, we suspect that this signal is due to residual nitrogen incorporated into the bulk of the ITO film, likely due to the preparation process. In contrast, the reference 2PACz spectrum displays a characteristic multi-peak structure, with the most prominent peak at ~398 eV (note that the intensity axis of this spectrum was multiplied by 0.15 to allow for better comparison of the spectral series in Figure 6A). We attribute this peak to the transition of an electron from the highest occupied molecular orbital, located at the nitrogen atom within the carbazole ring, into the N 1s core hole. Other peaks with lower emission energy can be associated with transitions from lower-lying molecular orbitals into the N 1s core hole.

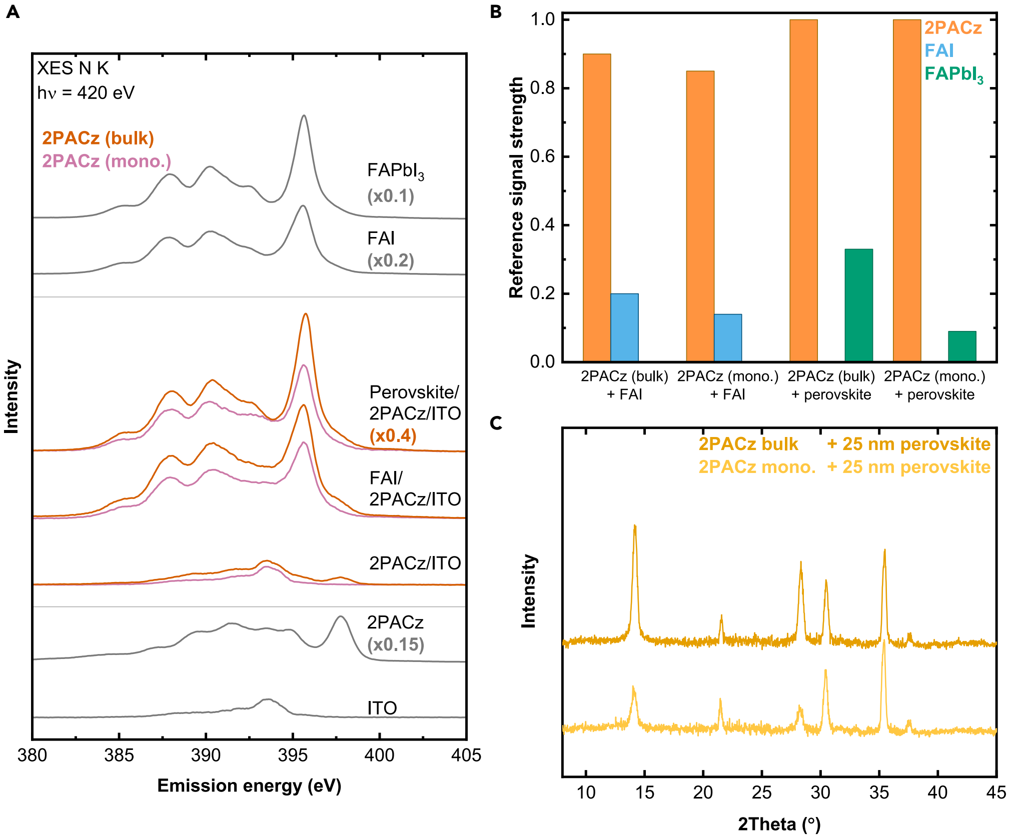

Figure 6. XES and thin-film XRD results indicating changes in perovskite and FAI deposition in thin films

(A) XES spectra of ~25-nm FAI and ~25-nm $Cs_{0.13}FA_{0.87}PbI_3$ perovskites deposited onto bulk or monolayer 2PACz films. Reference 2PACz (pressed powder pellet), ITO, FAI,[71] and $FAPbI_3$ spectra are also shown. Where necessary, spectra were multiplied by the given truncation factor for easier viewing.

(B) Overview of the signal contributions of respective reference fit components to the description of the spectra in (A). Note that these contributions are not precisely proportional to the nitrogen concentration due to possible differences in the photoionization cross-sections of the different compounds.

(C) XRD spectra of unannealed ~25-nm $Cs_{0.13}FA_{0.87}Pb(I_{0.95}Cl_{0.05})_3$ perovskite films deposited onto bulk or monolayer 2PACz films.

Both 2PACz substrate samples (labeled 2PACz/ITO in Figure 6A, bottom spectra in the center panel) need to be interpreted as a superposition of the ITO N K signal (main peak at ~394 eV) and the reference 2PACz spectrum (most prominent peak at ~398 eV). While bulk 2PACz can easily be reconstructed from a combination of ITO and 2PACz reference signals, the monolayer 2PACz/ITO substrate did not require a 2PACz contribution to reproduce the signal. The former suggests that the chemical structure of the evaporated 2PACz on ITO is equivalent to the powder reference, while the latter indicates that the 2PACz signal for the monolayer film is well below that of the ITO substrate and thus corroborates the finding of a very thin layer.

Upon FAI deposition, we observe the characteristic N K FAI spectral fingerprint (compare with the FAI reference spectra in Figure 6A, top panel, second from top).[71] Similarly, both samples with a 25-nm $FAPbI_3$ perovskite deposition (Figure 6A, center panel, top spectra) resemble the $FAPbI_3$ spectral fingerprint, which consists of the FA^+-ion and halide-derived hybrid orbitals (Figure 6A, top panel, top spectrum, ×0.1). For each pair of spectra, the bulk data show a significant higher intensity, especially for the $FAPbI_3$/2PACz/ITO samples (note the factor of ×0.4). To quantify the spectral contribution, we performed a fit analysis of the spectra using the respective 2PACz substrate signal and either the FAI or $FAPbI_3$ spectrum as fitting components. For the FAI spectra, the monolayer FAI spectrum can be reproduced using [0.85× 2PACz + 0.14× FAI] while the bulk spectrum required a larger FAI component [0.90× 2PACz + 0.20× FAI]. In the same fashion, perovskite growth rates follow this trend, i.e., [1.0× 2PACz + 0.09× perovskite] and [1.0× 2PACz + 0.35× perovskite] for monolayer and bulk 2PACz, respectively. This indicates a clear increase in crystalline perovskite growth rate, partially mediated by an increased affinity of FAI to adhere to bulk 2PACz. Notably, no large spectral changes are observed for the 2PACz SAMs after deposition of 25 nm CsI or PbI_2 (Figure S26). While some of the spectral features at the lower end of the valence region appear sharper after the deposition, the overall spectral shape is retained, indicating only weak (if any) interactions between these materials and the underlying 2PACz substrates.

XRD measurements of the samples with a ~25-nm-thick perovskite film support the findings from the XES measurements and DFT results (Figure 6C). Films grown on monolayer 2PACz exhibit pure α-$FAPbI_3$ growth in the thin-film region (even without annealing). This is exactly what is predicted by the DFT modeling discussed above, where α-$FAPbI_3$ is the more stable product in the thin-film region, especially when entropic effects are included. Furthermore, co-evaporated thin films grown on bulk 2PACz exhibit higher signal intensity than their monolayer counterparts, providing further evidence for the enhanced crystalline perovskite signal in the presence of exposed phosphonic acid functional groups.

Combined, the DFT, XES, and XRD results indicate a potential explanation for the lower required FAI rates to form co-evaporated perovskites on SAM-HTLs with exposed phosphonic acid functional groups. The presence of exposed phosphonic acid functional groups enhances FAI adhesion to the surface, resulting in less FAI required to form a perovskite. Increased stability of the co-evaporated perovskite, mediated by NCIs between the perovskite surface and exposed phosphonic acid functional groups, promotes the formation and stabilization of crystalline perovskite. Formation of perovskite under exposure to excess cations has also been correlated to increased formation of α-$FAPbI_3$, which will further reinforce this preferential growth.[72] Abzieher et al. and Yan et al. demonstrated that initial perovskite growth conditions readily continue to propagate during film deposition to inform bulk properties.[20,23] Hence, the initial α-phase crystalline perovskite favors rapid crystallization and exhibits increased affinity to organic cations. This initial perovskite would persist into the bulk, explaining the change in required organic cation deposition rate. With this finding, our work thus deepens the previous understanding of the complex interplay between substrate surfaces and perovskite film growth, revealing how functional groups can be a driver for initial growth conditions that radically change film formation.

Conclusion

This work combines novel theoretical and experimental analyses of phosphonic acid surface interactions with co-evaporated perovskite films, furthering the understanding of substrate impact on evaporated perovskite crystal formation. The presence of interfacial phosphonic acid decreases the organic cation amount required to form stoichiometric films by ~23%–45%, depending on the employed SAM-HTL material. Furthermore, analysis of perovskite growth on various phosphonic acid-containing HTLs indicates that phosphonic acids suppress δ-$FAPbI_3$ and crystalline PbI_2 formation while promoting columnar growth (as indicated by a substantial change in

Please cite this article in press as: Feeney et al., Understanding and exploiting interfacial interactions between phosphonic acid functional groups and co-evaporated perovskites, Matter (2024), https://doi.org/10.1016/j.matt.2024.02.004

relative XRD peak intensities). Using 4dPA as a source of exposed phosphonic acid functional groups, these observed XRD trends are replicated for monolayer SAMs.

These studies result in PV performances of 16.2% for unwashed and 17.0% for washed solution-processed 2PACz as HTL. To the best of our knowledge, this work is the first example of co-evaporated perovskites deposited onto evaporated SAM-HTLs, which achieved 16.0% for unwashed and 16.7% for washed samples in the case of 2PACz, reinforcing the potential for evaporation as a potential deposition method for upscaled perovskite PV. It is also the first to comparatively investigate the growth of co-evaporated perovskites on 2PACz and Me-4PACz in both evaporated and solution-processed forms.

DFT analysis of various perovskite/SAM combinations indicates that, although phosphonic acid binding interacts more strongly with δ-$FAPbI_3$ than with α-$FAPbI_3$, it serves as a trap for the α phase at the initial stages of crystal formation and creates a passivation barrier that inhibits conversion into δ-$FAPbI_3$. Phosphonic acids strongly align to interact with interfacial iodine groups in the $FAPbI_3$ layer, an observation confirmed through liquid-phase NMR of interactions between 2PACz and the common organic cations of MAI, FAI, and GAI. Our mechanistic explanation is confirmed for FA-based evaporated perovskite thin films through XES analysis of evaporated perovskite films grown on 2PACz, both with and without exposed phosphonic acid functional groups. XES indicates a greater affinity of FAI to phosphonic acid terminated surfaces, and a greater crystalline perovskite signal, which would be expected by the discovered surface passivation effect. Our findings provide a potential explanation for the shift in required FAI rates based on surface functionalization. This work therefore shows the unique capacity of co-evaporated perovskites in exploiting surface functionalization to control growth characteristics, optimal FAI rate, and device PCE, highlighting and demonstrating the potential for rational design of substrates to influence organic cation rates through surface functionalization.

EXPERIMENTAL PROCEDURES

Resource availability

Lead contact

More information and requests for resources should be directed to and will be fulfilled by the lead contact, Paul Fassl (paul.fassl@kit.edu).

Materials availability

This study did not produce new unique materials.

Data and code availability

This study did not generate code. The data has been deposited at the KITopen repository under a CC-BY 4.0 Creative Commons Attribution Only license: KITopen (2024), https://doi.org/10.35097/1946.

Evaporation of self-assembled monolayer thin films

Evaporated nPACz (2PACz, MeO-2PACz, or Me-4PACz, from TCI) thin films were fabricated via physical vapor deposition from a crucible in a thermal evaporation system (Creaphys, OPTIvap) in a manner similar to our previously described method.[29] All films were deposited at pressures of approximately 5×10^{-6} mbar, with rates of 0.15–0.25 Å s^{-1} measured using a QCM. SAM-HTLs denoted as ''bulk films'' had a final (measured) thickness of 4 nm.

Solution-processed SAM thin films

SAM solutions were prepared by dissolving nPACz powders (2PACz, MeO-2PACz, or Me-4PACz, from TCI) in ethanol (Sigma-Aldrich, anhydrous) to create solutions with concentrations of 2.98 mM. Solutions were ultrasonicated for 30 min to equilibrate.

Solution-processed SAM-HTLs were deposited using a one-step spin-coating program (3,000 rpm for 30 s) with 70 μL of solution in a nitrogen glovebox. Films were then dried at 100°C for 10 min.

Washing of SAM thin films

A select subset of SAM-HTLs (labeled "monolayer films" in this work) were washed using a one-step spin-coating program (3,000 rpm for 30 s) and 150 μL of ethanol (Sigma-Aldrich, anhydrous), dynamically added after 10 s. Washed films were dried at 100°C for a further 10 min.

Fabrication of perovskite solar cells

Planar p-i-n PSCs were fabricated with the architecture of glass/ITO/SAM-HTL/$Cs_{0.13}FA_{0.87}Pb(I_{0.95}Cl_{0.05})_3$/$C_{60}$/$SnO_x$/Au. ITO substrates (15 Ω/sq, Luminescence Technology) were cut to sizes of 0.16 cm × 0.16 cm and cleaned with acetone and isopropanol in an ultrasonic bath for 15 min each. Substrates were treated with oxygen plasma for 3 min immediately prior to deposition of the SAM-HTLs.

For perovskite deposition, a nitrogen glovebox integrated PEROvap (CreaPhys) evaporator was employed. Four QCMs were used to measure the rate of each material independently. A cooling inner surface, surrounding all evaporation sources, was set to −25°C. Prior to the heating process, the system was evacuated for 60 min, with a standard base pressure at start of heating of 3×10^{-6} mbar. For every process, the evaporation rate of each material was kept constant by manually adjusting the source temperature. Substrate temperature (18°C) and substrate rotation speed (10 rpm) were held constant for all experiments. Inorganic rates during evaporation were $PbI_2 = 0.23$ Å s^{-1}, CsI = 0.025 Å s^{-1}, and $PbCl_2 = 0.01$ Å s^{-1}. As discussed in this work, FAI incorporation and adhesion is strongly dependent on the substrate and underlying material. For this reason, the tooling factor and rates of FAI are somewhat arbitrary. The tooling factor and rates for this recipe were originally optimized for an FAI rate of 1.0 Å s^{-1}, which was the optimal rate (in terms of PV performance) for washed 2PACz as HTL at that time. The "equivalent FAI rate," as shown, e.g., in Figure 2, is based on this initially optimized rate. FAI is known to exhibit decomposition at high temperatures and is suspected to exhibit a variable tooling factor dependent on rate due to local pressure.[45] To prevent such effects over the large variation in FAI rates required, a variation in perovskite stoichiometry was achieved by keeping the FAI rate below or close to the equivalent FAI rate of ~1 Å s^{-1}. For a standard co-evaporation of a 550-nm perovskite layer, deposition time was approximately 180 min. All samples were annealed at 140°C for 10 min in nitrogen atmosphere at ambient pressure.

An ETL, comprising 20 nm fullerene (C_{60}, Alfa Aesar), was thermally evaporated at a rate of 0.1–0.2 Å s^{-1} under a pressure of approximately 1×10^{-6} mbar in a vacuum evaporation system (CreaPhys, OPTIvap). SnO_x (35 nm) was deposited via atomic layer deposition, as described in our previous work.[73] All samples were completed with the evaporation of a 75-nm Au rear electrode, with an active area of 10.5 mm^2 defined via shadow mask.

Please cite this article in press as: Feeney et al., Understanding and exploiting interfacial interactions between phosphonic acid functional groups and co-evaporated perovskites, Matter (2024), https://doi.org/10.1016/j.matt.2024.02.004

Characterization methods

Current density-voltage measurements

J-V characteristics were measured using a class AAA solar simulator (Newport, Oriel Sol3A) at a power density of 100 mW cm^{-2}, calibrated using a reference silicon solar cell (Newport, calibrated 2018) equipped with a KG5 bandpass filter to simulate the AM 1.5G solar spectrum (Figure S27). Scan rate during measurement was set to 0.6 V s^{-1} using a source meter (Keithley, 2400 A). The stabilized PCE of PSCs was determined by tracking the MPP under continuous AM 1.5G illumination for 300 s. The solar cell temperature during measurements was actively regulated by a Peltier element connected to a microcontroller set to 25°C.

X-ray diffraction spectra

Crystal structure analysis of perovskite layers was carried out utilizing an XRD system (Bruker D2Phaser system) with Cu-K_α radiation (λ = 1.5405 Å) in Bragg-Brentano configuration using a LynxEye detector. XRD spectra were measured for perovskite layers deposited on substrates with unpatterned ITO and the stated HTL.

X-ray emission spectroscopy measurements

For XES, the samples were processed at KIT, sealed in dry nitrogen atmosphere, shipped to Beamline 8.0.1 at the Advanced Light Source, Lawrence Berkeley National Laboratory, and inserted into the SALSA endstation[74] without any air exposure. The N K emission spectra were recorded with a high-transmission soft X-ray spectrometer,[75] and the energy axis was calibrated using BN and $CaSO_4$.[76] 2PACz reference powder (TCI America, purity >98.0%) was pressed into a pellet in a nitrogen-filled glovebox. To mitigate X-ray beam-induced changes, all samples were scanned under the X-ray beam with a speed of 600 μm s^{-1}, which corresponds to an exposure time of 50 ms for each spot. Detailed studies were performed to ascertain that beam-induced changes observed in static measurements were absent in the data with sample scanning.

Nuclear magnetic resonance measurements

NMR spectra (^{1}H) were recorded in d6-DMSP at 400 MHz with a Bruker spectrometer at 298 K. Chemical shifts are reported in parts per million (ppm) relative to the traces of d5-DMSO (δ_H = 2.50 ppm) in the corresponding fully deuterated solvent. All materials were weighed out in a nitrogen-filled glovebox and mixed under ambient conditions.

Density functional theory calculations

Ab initio *computations*

Computations were performed using DFT as implemented in the quantum espresso package with PBE exchange-correlation functional.[77] The core electrons were modeled using ultrasoft pseudopotentials, a plane-wave basis set cutoff of 55 Ry was used, and the dispersion correction was included at the DFT-D3 level.[78] Relaxations of the structures were performed using the conjugate gradient methods with a convergence threshold on forces set to 10^{-3} (in atomic units).

Determination of entropic contribution

We utilized the entropy argument from Chen et al.[66] to explain the stability of α-$FAPbI_3$ above room temperature. If we assume that the formamidinium cation is geometrically restricted within the hexagonal δ-$FAPbI_3$ unit cell (in line with the X-ray analysis by Chen et al.[66]), the Gibbs free energy of δ-$FAPbI_3$ is equal to its total internal energy, namely

$$G^{\delta} = E^{\delta}_{\mathrm{DFT}}.$$

For the cubic α-$FAPbI_3$, the X-ray data clearly indicate a random rotation of the FA^+ within the cubic unit cell. Consequently, this free and random motion will result in an entropy contribution to the Gibbs free energy of the α-$FAPbI_3$:

$$G^{\alpha} = E^{\alpha}_{\mathrm{DFT}} - T \times S,$$

where T is the temperature and S is the entropy of FA^+ equal to

$$S = \frac{3}{2}k_B \times \left\{1 + \ln\left(0.478 \times k_B T \times (I_1 I_2 I_3)^{\frac{1}{3}}\right)\right\}.$$

In the above expression, k_B and T are the Boltzmann constant and temperature, respectively, and the principal moments of inertia I_i of FA^+ are 11.644, 60.161, and 71.806 u Å, where the unified atomic mass unit, u, is 1.6605×10^{-27} kg.[66] At T = 18°C, the entropy contribution amounts to −253 meV.

SUPPLEMENTAL INFORMATION

Supplemental information can be found online at https://doi.org/10.1016/j.matt.2024.02.004.

ACKNOWLEDGMENTS

The authors gratefully acknowledge financial support by the initiating and networking funding of the Helmholtz Association (HYIG of U.W.P. [VHNG-1148]), the Helmholtz Energy Materials Foundry, the German Federal Ministry for Economic Affairs and Climate Action (BMWK) through the project 27Plus6 (03EE1056B) as well as project SHAPE (03EE1123A), funding from the European Commission Horizon Europe research and innovation program under the NEXUS grant (101075330), and the Karlsruhe School of Optics and Photonics. The authors acknowledge the Helmholtz Association (program-oriented funding IV, Materials and Technologies for the Energy Transition, Topic 1: Photovoltaics and Wind Energy, Code: 38.01.02). The authors also acknowledge the Karlsruhe Micro Nano Facility, which provided access for atomic layer deposition, and thank Dr. Andreas Rapp, Despina Savviduo, and Tanja Ohmer-Scherrer for their support in measuring NMR data presented herein. A.T., M.E., and G.G. gratefully acknowledge support from the Klaus Tschira Foundation, funding from the European Research Council under the European Union's Horizon 2020 research and innovation program (grant agreement no. 101042290 PATTERNCHEM), and the computing time provided to them on the high-performance computer Noctua 2 under the project hpc-prf-patchem at the NHR Center PC2, funded by the Federal Ministry of Education and Research and the state governments participating on the basis of the resolutions of the GWK for national high-performance computing at universities (www.nhr-verein.de/unsere-partner). This research used resources of the Advanced Light Source, which is a DOE Office of Science User Facility under contract no. DE-AC02-05CH11231.

AUTHOR CONTRIBUTIONS

T.F. conceived the initial idea for this study and developed it further with the support of J.P. T.F. fabricated the presented thin-film samples; performed and analyzed JV, EQE, MPP, XRD, and PLQY measurements; and analyzed TCSPC measurements. J.P. was heavily involved in sample fabrication confirming initial concepts, assisted in experimental design, and performed and analyzed all NMR measurements. A.T., M.E., and G.G. performed and analyzed all DFT calculations. D.H., C.W., C.H., and L.W. performed and analyzed all XES measurements. B.H. performed all TCSPC measurements and assisted in the fitting routine. A.D. was involved in

Please cite this article in press as: Feeney et al., Understanding and exploiting interfacial interactions between phosphonic acid functional groups and co-evaporated perovskites, Matter (2024), https://doi.org/10.1016/j.matt.2024.02.004

sample fabrication confirming initial concepts, provided valuable discussions, and performed all SEM measurements. P.F. and U.W.P. provided valuable discussion and supervised the project. T.F. drafted the manuscript with the support of J.P., A.T., and D.H., and the manuscript was written through contributions of all authors. All authors reviewed and commented on the paper.

DECLARATION OF INTERESTS

The authors declare no competing interests.

Received: October 20, 2023
Revised: January 4, 2024
Accepted: February 7, 2024
Published: March 8, 2024

REFERENCES

1. Zuo, C., Bolink, H.J., Han, H., Huang, J., Cahen, D., and Ding, L. (2016). Advances in Perovskite Solar Cells. Adv. Sci. *3*, 1500324. https://doi.org/10.1002/advs.201500324.
2. De Wolf, S., Holovsky, J., Moon, S.-J., Löper, P., Niesen, B., Ledinsky, M., Haug, F.-J., Yum, J.-H., and Ballif, C. (2014). Organometallic Halide Perovskites: Sharp Optical Absorption Edge and Its Relation to Photovoltaic Performance. J. Phys. Chem. Lett. *5*, 1035–1039. https://doi.org/10.1021/jz500279b.
3. Xing, G., Mathews, N., Sun, S., Lim, S.S., Lam, Y.M., Grätzel, M., Mhaisalkar, S., and Sum, T.C. (2013). Long-Range Balanced Electron- and Hole-Transport Lengths in Organic-Inorganic $CH_3NH_3PbI_3$. Science *342*, 344–347. https://doi.org/10.1126/science.1243167.
4. Li, Z., Li, B., Wu, X., Sheppard, S.A., Zhang, S., Gao, D., Long, N.J., and Zhu, Z. (2022). Organometallic-functionalized interfaces for highly efficient inverted perovskite solar cells. Science *376*, 416–420. https://doi.org/10.1126/science.abm8566.
5. Kim, M., Jeong, J., Lu, H., Lee, T.K., Eickemeyer, F.T., Liu, Y., Choi, I.W., Choi, S.J., Jo, Y., Kim, H.-B., et al. (2022). Conformal quantum dot–SnO_2 layers as electron transporters for efficient perovskite solar cells. Science *375*, 302–306. https://doi.org/10.1126/science.abh1885.
6. Ruiz-Preciado, M.A., Gota, F., Fassl, P., Hossain, I.M., Singh, R., Laufer, F., Schackmar, F., Feeney, T., Farag, A., Allegro, I., et al. (2022). Monolithic Two-Terminal Perovskite/CIS Tandem Solar Cells with Efficiency Approaching 25%. ACS Energy Lett. *7*, 2273–2281. https://doi.org/10.1021/acsenergylett.2c00707.
7. Al-Ashouri, A., Magomedov, A., Roß, M., Jošt, M., Talaikis, M., Chistiakova, G., Bertram, T., Márquez, J.A., Köhnen, E., Kasparavičius, E., et al. (2019). Conformal monolayer contacts with lossless interfaces for perovskite single junction and monolithic tandem solar cells. Energy Environ. Sci. *12*, 3356–3369. https://doi.org/10.1039/C9EE02268F.
8. Yang, G., Ren, Z., Liu, K., Qin, M., Deng, W., Zhang, H., Wang, H., Liang, J., Ye, F., Liang, Q., et al. (2021). Stable and low-photovoltage-loss perovskite solar cells by multifunctional passivation. Nat. Photonics *15*, 681–689. https://doi.org/10.1038/s41566-021-00829-4.
9. Li, B., and Zhang, W. (2022). Improving the stability of inverted perovskite solar cells towards commercialization. Commun. Mater. *3*, 65. https://doi.org/10.1038/s43246-022-00291-x.
10. Mei, A., Sheng, Y., Ming, Y., Hu, Y., Rong, Y., Zhang, W., Luo, S., Na, G., Tian, C., Hou, X., et al. (2020). Stabilizing Perovskite Solar Cells to IEC61215:2016 Standards with over 9,000-h Operational Tracking. Joule *4*, 2646–2660. https://doi.org/10.1016/j.joule.2020.09.010.
11. Kang, Y., Wang, A., Li, R., Song, Y., Wang, X., Li, H., Xu, W., Zhang, L., and Dong, Q. (2022). Thermal Shock Fabrication of Ion-Stabilized Perovskite and Solar Cells. Adv. Mater. *34*, 2203166. https://doi.org/10.1002/adma.202203166.
12. Vaynzof, Y. (2020). The Future of Perovskite Photovoltaics—Thermal Evaporation or Solution Processing? Adv. Energy Mater. *10*, 2003073. https://doi.org/10.1002/aenm.202003073.
13. Howard, I.A., Abzieher, T., Hossain, I.M., Eggers, H., Schackmar, F., Ternes, S., Richards, B.S., Lemmer, U., and Paetzold, U.W. (2019). Coated and Printed Perovskites for Photovoltaic Applications. Adv. Mater. *31*, 1806702. https://doi.org/10.1002/adma.201806702.
14. Ritzer, D.B., Abzieher, T., Basibüyük, A., Feeney, T., Laufer, F., Ternes, S., Richards, B.S., Bergfeld, S., and Paetzold, U.W. (2022). Upscaling of perovskite solar modules: The synergy of fully evaporated layer fabrication and all-laser-scribed interconnections. Progress in Photovoltaics *30*, 360–373. https://doi.org/10.1002/pip.3489.
15. Paliwal, A., Zanoni, K.P., Roldán-Carmona, C., Hernández-Fenollosa, M.A., and Bolink, H.J. (2023). Fully vacuum-deposited perovskite solar cells in substrate configuration. Matter *6*, 3499–3508. https://doi.org/10.1016/j.matt.2023.07.011.
16. Kosasih, F.U., Erdenebileg, E., Mathews, N., Mhaisalkar, S.G., and Bruno, A. (2022). Thermal evaporation and hybrid deposition of perovskite solar cells and mini-modules. Joule *6*, 2692–2734. https://doi.org/10.1016/j.joule.2022.11.004.
17. Gil-Escrig, L., Momblona, C., La-Placa, M.-G., Boix, P.P., Sessolo, M., and Bolink, H.J. (2018). Vacuum Deposited Triple-Cation Mixed-Halide Perovskite Solar Cells. Adv. Energy Mater. *8*, 1703506. https://doi.org/10.1002/aenm.201703506.
18. Susic, I., Kama, A., Gil-Escrig, L., Dreessen, C., Palazon, F., Cahen, D., Sessolo, M., and Bolink, H.J. (2023). Combinatorial Vacuum-Deposition of Wide Bandgap Perovskite Films and Solar Cells. Adv. Mater. Interfaces *10*, 2202271. https://doi.org/10.1002/admi.202202271.
19. Longo, G., Momblona, C., La-Placa, M.-G., Gil-Escrig, L., Sessolo, M., and Bolink, H.J. (2018). Fully Vacuum-Processed Wide Band Gap Mixed-Halide Perovskite Solar Cells. ACS Energy Lett. *3*, 214–219. https://doi.org/10.1021/acsenergylett.7b01217.
20. Yan, S., Patel, J.B., Lee, J.E., Elmestekawy, K.A., Ratnasingham, S.R., Yuan, Q., Herz, L.M., Noel, N.K., and Johnston, M.B. (2023). A Templating Approach to Controlling the Growth of Coevaporated Halide Perovskites. ACS Energy Lett. *8*, 4008–4015. https://doi.org/10.1021/acsenergylett.3c01368.
21. Olthof, S., and Meerholz, K. (2017). Substrate-dependent electronic structure and film formation of $MAPbI_3$ perovskites. Sci. Rep. *7*, 40267. https://doi.org/10.1038/srep40267.
22. Shallcross, R.C., Olthof, S., Meerholz, K., and Armstrong, N.R. (2019). Impact of Titanium Dioxide Surface Defects on the Interfacial Composition and Energetics of Evaporated Perovskite Active Layers. ACS Appl. Mater. Interfaces *11*, 32500–32508. https://doi.org/10.1021/acsami.9b09935.
23. Abzieher, T., Feeney, T., Schackmar, F., Donie, Y.J., Hossain, I.M., Schwenzer, J.A., Hellmann, T., Mayer, T., Powalla, M., and Paetzold, U.W. (2021). From Groundwork to Efficient Solar Cells: On the Importance of the Substrate Material in Co-Evaporated Perovskite Solar Cells. Adv. Funct. Mater. *31*, 2104482. https://doi.org/10.1002/adfm.202104482.
24. Roß, M., Severin, S., Stutz, M.B., Wagner, P., Köbler, H., Favin-Lévêque, M., Al-Ashouri, A., Korb, P., Tockhorn, P., Abate, A., et al. (2021).

Co-Evaporated Formamidinium Lead Iodide Based Perovskites with 1000 h Constant Stability for Fully Textured Monolithic Perovskite/Silicon Tandem Solar Cells. Adv. Energy Mater. *11*, 2101460. https://doi.org/10.1002/aenm.202101460.

25. Roß, M., Gil-Escrig, L., Al-Ashouri, A., Tockhorn, P., Jošt, M., Rech, B., and Albrecht, S. (2020). Co-Evaporated p-i-n Perovskite Solar Cells beyond 20% Efficiency: Impact of Substrate Temperature and Hole-Transport Layer. ACS Appl. Mater. Interfaces *12*, 39261–39272. https://doi.org/10.1021/acsami.0c10898.

26. Klipfel, N., Momblona, C., Kanda, H., Shibayama, N., Nakamura, Y., Mensi, M.D., Liu, C., Roldán-Carmona, C., and Nazeeruddin, M.K. (2021). Crystallographically Oriented Hybrid Perovskites via Thermal Vacuum Codeposition. Sol. RRL *5*, 2100191. https://doi.org/10.1002/solr.202100191.

27. Gallet, T., Poeira, R.G., Lanzoni, E.M., Abzieher, T., Paetzold, U.W., and Redinger, A. (2021). Co-evaporation of $CH_3NH_3PbI_3$: How Growth Conditions Impact Phase Purity, Photostriction, and Intrinsic Stability. ACS Appl. Mater. Interfaces *13*, 2642–2653. https://doi.org/10.1021/acsami.0c19038.

28. Schreiber, F. (2000). Structure and growth of self-assembling monolayers. Prog. Surf. Sci. *65*, 151–257. https://doi.org/10.1016/S0079-6816(00)00024-1.

29. Farag, A., Feeney, T., Hossain, I.M., Schackmar, F., Fassl, P., Küster, K., Bäuerle, R., Ruiz-Preciado, M.A., Hentschel, M., Ritzer, D.B., et al. (2023). Evaporated Self-Assembled Monolayer Hole Transport Layers: Lossless Interfaces in p-i-n Perovskite Solar Cells. Adv. Energy Mater. *13*, 2203982. https://doi.org/10.1002/aenm.202203982.

30. Zhang, Z., Fang, Z., Guo, T., Zhao, R., Deng, Z., Zhang, J., Shang, M., Liu, X., Liu, J., Huang, L., et al. (2022). Robust heterojunction to strengthen the performances of FAPbI3 perovskite solar cells. Chem. Eng. J. *432*, 134311. https://doi.org/10.1016/j.cej.2021.134311.

31. Paniagua, S.A., Giordano, A.J., Smith, O.L., Barlow, S., Li, H., Armstrong, N.R., Pemberton, J.E., Brédas, J.-L., Ginger, D., and Marder, S.R. (2016). Phosphonic Acids for Interfacial Engineering of Transparent Conductive Oxides. Chem. Rev. *116*, 7117–7158. https://doi.org/10.1021/acs.chemrev.6b00061.

32. Xie, H., Wang, Z., Chen, Z., Pereyra, C., Pols, M., Gałkowski, K., Anaya, M., Fu, S., Jia, X., Tang, P., et al. (2021). Decoupling the effects of defects on efficiency and stability through phosphonates in stable halide perovskite solar cells. Joule *5*, 1246–1266. https://doi.org/10.1016/j.joule.2021.04.003.

33. Gharibzadeh, S., Fassl, P., Hossain, I.M., Rohrbeck, P., Frericks, M., Schmidt, M., Duong, T., Khan, M.R., Abzieher, T., Nejand, B.A., et al. (2021). Two birds with one stone: dual grain-boundary and interface passivation enables >22% efficient inverted methylammonium-free perovskite solar cells. Energy Environ. Sci. *14*, 5875–5893. https://doi.org/10.1039/D1EE01508G.

34. Lohmann, K.B., Motti, S.G., Oliver, R.D.J., Ramadan, A.J., Sansom, H.C., Yuan, Q., Elmestekawy, K.A., Patel, J.B., Ball, J.M., Herz, L.M., et al. (2022). Solvent-Free Method for Defect Reduction and Improved Performance of p-i-n Vapor-Deposited Perovskite Solar Cells. ACS Energy Lett. *7*, 1903–1911. https://doi.org/10.1021/acsenergylett.2c00865.

35. Pitaro, M., Alonso, J.E.S., Di Mario, L., Romero, D.G., Tran, K., Kardula, J., Zaharia, T., Johansson, M.B., Johansson, E.M.J., Chiechi, R.C., and Loi, M.A. (2023). Tuning the Surface Energy of Hole Transport Layers Based on Carbazole Self-Assembled Monolayers for Highly Efficient Sn/Pb Perovskite Solar Cells. Adv. Funct. Mater. 2306571. https://doi.org/10.1002/adfm.202306571.

36. Sinnokrot, M.O., and Sherrill, C.D. (2004). Substituent Effects in $\pi-\pi$ Interactions: Sandwich and T-Shaped Configurations. J. Am. Chem. Soc. *126*, 7690–7697. https://doi.org/10.1021/ja049434a.

37. Aliakbar Tehrani, Z., and Kim, K.S. (2016). Functional molecules and materials by π-Interaction based quantum theoretical design. Int. J. Quantum Chem. *116*, 622–633. https://doi.org/10.1002/qua.25109.

38. Saliba, M., and Etgar, L. (2020). Current Density Mismatch in Perovskite Solar Cells. ACS Energy Lett. *5*, 2886–2888. https://doi.org/10.1021/acsenergylett.0c01642.

39. Thiesbrummel, J., Le Corre, V.M., Peña-Camargo, F., Perdigón-Toro, L., Lang, F., Yang, F., Grischek, M., Gutierrez-Partida, E., Warby, J., Farrar, M.D., et al. (2021). Universal Current Losses in Perovskite Solar Cells Due to Mobile Ions. Adv. Energy Mater. *11*, 2101447. https://doi.org/10.1002/aenm.202101447.

40. Xu, W., Hart, L.J.F., Moss, B., Caprioglio, P., Macdonald, T.J., Furlan, F., Panidi, J., Oliver, R.D.J., Pacalaj, R.A., Heeney, M., et al. (2023). Impact of Interface Energetic Alignment and Mobile Ions on Charge Carrier Accumulation and Extraction in p-i-n Perovskite Solar Cells. Adv. Energy Mater. *13*, 2301102. https://doi.org/10.1002/aenm.202301102.

41. Ye, F., Zhang, S., Warby, J., Wu, J., Gutierrez-Partida, E., Lang, F., Shah, S., Saglamkaya, E., Sun, B., Zu, F., et al. (2022). Overcoming C60-induced interfacial recombination in inverted perovskite solar cells by electron-transporting carborane. Nat. Commun. *13*, 7454. https://doi.org/10.1038/s41467-022-34203-x.

42. de Quilettes, D.W., Vorpahl, S.M., Stranks, S.D., Nagaoka, H., Eperon, G.E., Ziffer, M.E., Snaith, H.J., and Ginger, D.S. (2015). Impact of microstructure on local carrier lifetime in perovskite solar cells. Science *348*, 683–686. https://doi.org/10.1126/science.aaa5333.

43. Péan, E.V., Dimitrov, S., De Castro, C.S., and Davies, M.L. (2020). Interpreting time-resolved photoluminescence of perovskite materials. Phys. Chem. Chem. Phys. *22*, 28345–28358. https://doi.org/10.1039/D0CP04950F.

44. Oliver, R.D.J., Caprioglio, P., Peña-Camargo, F., Buizza, L.R.V., Zu, F., Ramadan, A.J., Motti, S.G., Mahesh, S., McCarthy, M.M., Warby, J.H., et al. (2022). Understanding and suppressing non-radiative losses in methylammonium-free wide-bandgap perovskite solar cells. Energy Environ. Sci. *15*, 714–726. https://doi.org/10.1039/D1EE02650J.

45. Kroll, M., Öz, S.D., Zhang, Z., Ji, R., Schramm, T., Antrack, T., Vaynzof, Y., Olthof, S., and Leo, K. (2022). Insights into the evaporation behaviour of FAI: material degradation and consequences for perovskite solar cells. Sustain. Energy Fuels *6*, 3230–3239. https://doi.org/10.1039/D2SE00373B.

46. Wang, Q., Shao, Y., Xie, H., Lyu, L., Liu, X., Gao, Y., and Huang, J. (2014). Qualifying composition dependent p and n self-doping in $CH_3NH_3PbI_3$. Appl. Phys. Lett. *105*, 163508. https://doi.org/10.1063/1.4899051.

47. Fassl, P., Lami, V., Bausch, A., Wang, Z., Klug, M.T., Snaith, H.J., and Vaynzof, Y. (2018). Fractional deviations in precursor stoichiometry dictate the properties, performance and stability of perovskite photovoltaic devices. Energy Environ. Sci. *11*, 3380–3391. https://doi.org/10.1039/C8EE01136B.

48. Zhou, N., Shen, Y., Zhang, Y., Xu, Z., Zheng, G., Li, L., Chen, Q., and Zhou, H. (2017). CsI Pre-Intercalation in the Inorganic Framework for Efficient and Stable $FA_{1-x}Cs_xPbI_3(Cl)$ Perovskite Solar Cells. Small *13*, 1700484. https://doi.org/10.1002/smll.201700484.

49. Sun, Y., Chen, H., Zhang, T., and Wang, D. (2018). Chemical state of chlorine in perovskite solar cell and its effect on the photovoltaic performance. J. Mater. Sci. *53*, 13976–13986. https://doi.org/10.1007/s10853-018-2571-2.

50. Yi, C., Luo, J., Meloni, S., Boziki, A., Ashari-Astani, N., Grätzel, C., Zakeeruddin, S.M., Röthlisberger, U., and Grätzel, M. (2016). Entropic stabilization of mixed A-cation ABX_3 metal halide perovskites for high performance perovskite solar cells. Energy Environ. Sci. *9*, 656–662. https://doi.org/10.1039/C5EE03255E.

51. Tockhorn, P., Sutter, J., Cruz, A., Wagner, P., Jäger, K., Yoo, D., Lang, F., Grischek, M., Li, B., Li, J., et al. (2022). Nano-optical designs for high-efficiency monolithic perovskite–silicon tandem solar cells. Nat. Nanotechnol. *17*, 1214–1221. https://doi.org/10.1038/s41565-022-01228-8.

52. Jošt, M., Köhnen, E., Al-Ashouri, A., Bertram, T., Tomšič, Š., Magomedov, A., Kasparavicius, E., Kodalle, T., Lipovšek, B., Getautis, V., et al. (2022). Perovskite/CIGS Tandem Solar Cells: From Certified 24.2% toward 30% and Beyond. ACS Energy Lett. *7*, 1298–1307. https://doi.org/10.1021/acsenergylett.2c00274.

53. Al-Ashouri, A., Marčinskas, M., Kasparavičius, E., Malinauskas, T., Palmstrom, A., Getautis, V., Albrecht, S., McGehee, M.D., and Magomedov, A. (2023). Wettability Improvement of a Carbazole-Based Hole-Selective Monolayer for Reproducible Perovskite Solar Cells. ACS Energy Lett. *8*, 898–900. https://doi.org/10.1021/acsenergylett.2c02629.

54. Hossain, K., Kulkarni, A., Bothra, U., Klingebiel, B., Kirchartz, T., Saliba, M., and Kabra, D. (2023). Resolving the Hydrophobicity of the Me-4PACz Hole Transport Layer for Inverted Perovskite Solar Cells with Efficiency >20%. ACS Energy Lett. *8*, 3860–3867. https://doi.org/10.1021/acsenergylett.3c01385.

55. Liu, M., Bi, L., Jiang, W., Zeng, Z., Tsang, S.-W., Lin, F.R., and Jen, A.K.-Y. (2023). Compact Hole-Selective Self-Assembled Monolayers Enabled by Disassembling Micelles in Solution for Efficient Perovskite Solar Cells. Adv. Mater. *35*, 2304415. https://doi.org/10.1002/adma.202304415.

56. Jacobsson, T.J., Correa-Baena, J.P., Halvani Anaraki, E., Philippe, B., Stranks, S.D., Bouduban, M.E.F., Tress, W., Schenk, K., Teuscher, J., Moser, J.E., et al. (2016). Unreacted PbI_2 as a Double-Edged Sword for Enhancing the Performance of Perovskite Solar Cells. J. Am. Chem. Soc. *138*, 10331–10343. https://doi.org/10.1021/jacs.6b06320.

57. Van Gompel, W.T.M., Herckens, R., Reekmans, G., Ruttens, B., D'Haen, J., Adriaensens, P., Lutsen, L., and Vanderzande, D. (2018). Degradation of the Formamidinium Cation and the Quantification of the Formamidinium–Methylammonium Ratio in Lead Iodide Hybrid Perovskites by Nuclear Magnetic Resonance Spectroscopy. J. Phys. Chem. C *122*, 4117–4124. https://doi.org/10.1021/acs.jpcc.7b09805.

58. Kuang, C., Hu, Z., Yuan, Z., Wen, K., Qing, J., Kobera, L., Abbrent, S., Brus, J., Yin, C., Wang, H., et al. (2021). Critical role of additive-induced molecular interaction on the operational stability of perovskite light-emitting diodes. Joule *5*, 618–630. https://doi.org/10.1016/j.joule.2021.01.003.

59. Charisiadis, P., Kontogianni, V.G., Tsiafoulis, C.G., Tzakos, A.G., Siskos, M., and Gerothanassis, I.P. (2014). 1H-NMR as a Structural and Analytical Tool of Intra- and Intermolecular Hydrogen Bonds of Phenol-Containing Natural Products and Model Compounds. Molecules *19*, 13643–13682. https://doi.org/10.3390/molecules190913643.

60. Li, X., Dar, M.I., Yi, C., Luo, J., Tschumi, M., Zakeeruddin, S.M., Nazeeruddin, M.K., Han, H., and Grätzel, M. (2015). Improved performance and stability of perovskite solar cells by crystal crosslinking with alkylphosphonic acid ω-ammonium chlorides. Nat. Chem. *7*, 703–711. https://doi.org/10.1038/nchem.2324.

61. Fabini, D.H., Stoumpos, C.C., Laurita, G., Kaltzoglou, A., Kontos, A.G., Falaras, P., Kanatzidis, M.G., and Seshadri, R. (2016). Reentrant Structural and Optical Properties and Large Positive Thermal Expansion in Perovskite Formamidinium Lead Iodide. Angew. Chem. Int. Ed. Engl. *55*, 15392–15396. https://doi.org/10.1002/anie.201609538.

62. Costa, J.C.S., Azevedo, J., Santos, L.M.N.B.F., and Mendes, A. (2017). On the Deposition of Lead Halide Perovskite Precursors by Physical Vapor Method. J. Phys. Chem. C *121*, 2080–2087. https://doi.org/10.1021/acs.jpcc.6b11625.

63. Ehlert, C., Piras, A., and Gryn'ova, G. (2023). CO_2 on Graphene: Benchmarking Computational Approaches to Noncovalent Interactions. ACS Omega *8*, 35768–35778. https://doi.org/10.1021/acsomega.3c03251.

64. Vicent-Luna, J.M., Apergi, S., and Tao, S. (2021). Efficient Computation of Structural and Electronic Properties of Halide Perovskites Using Density Functional Tight Binding: GFN1-xTB Method. J. Chem. Inf. Model. *61*, 4415–4424. https://doi.org/10.1021/acs.jcim.1c00432.

65. Marín-Villa, P., Arauzo, A., Drużbicki, K., and Fernandez-Alonso, F. (2022). Unraveling the Ordered Phase of the Quintessential Hybrid Perovskite $MAPbI_3$—Thermophysics to the Rescue. J. Phys. Chem. Lett. *13*, 8422–8428. https://doi.org/10.1021/acs.jpclett.2c02208.

66. Chen, T., Foley, B.J., Park, C., Brown, C.M., Harriger, L.W., Lee, J., Ruff, J., Yoon, M., Choi, J.J., and Lee, S.-H. (2016). Entropy-driven structural transition and kinetic trapping in formamidinium lead iodide perovskite. Sci. Adv. *2*, e1601650. https://doi.org/10.1126/sciadv.1601650.

67. Zheng, Z., Wang, S., Hu, Y., Rong, Y., Mei, A., and Han, H. (2022). Development of formamidinium lead iodide-based perovskite solar cells: efficiency and stability. Chem. Sci. *13*, 2167–2183. https://doi.org/10.1039/D1SC04769H.

68. Fu, Y., Wu, T., Wang, J., Zhai, J., Shearer, M.J., Zhao, Y., Hamers, R.J., Kan, E., Deng, K., Zhu, X.-Y., and Jin, S. (2017). Stabilization of the Metastable Lead Iodide Perovskite Phase via Surface Functionalization. Nano Lett. *17*, 4405–4414. https://doi.org/10.1021/acs.nanolett.7b01500.

69. Chen, T., Xie, J., Wen, B., Yin, Q., Lin, R., Zhu, S., and Gao, P. (2023). Inhibition of defect-induced α-to-δ phase transition for efficient and stable formamidinium perovskite solar cells. Nat. Commun. *14*, 6125. https://doi.org/10.1038/s41467-023-41853-y.

70. Hauschild, D., Seitz, L., Gharibzadeh, S., Steininger, R., Jiang, N., Yang, W., Paetzold, U.W., Heske, C., and Weinhardt, L. (2021). Impact of n-Butylammonium Bromide on the Chemical and Electronic Structure of Double-Cation Perovskite Thin Films. ACS Appl. Mater. Interfaces *13*, 53202–53210. https://doi.org/10.1021/acsami.1c15707.

71. Kamal, C., Hauschild, D., Seitz, L., Steininger, R., Yang, W., Heske, C., Weinhardt, L., and Odelius, M. (2021). Coupling Methylammonium and Formamidinium Cations with Halide Anions: Hybrid Orbitals, Hydrogen Bonding, and the Role of Dynamics. J. Phys. Chem. C *125*, 25917–25926. https://doi.org/10.1021/acs.jpcc.1c08932.

72. Ma, F., Li, J., Li, W., Lin, N., Wang, L., and Qiao, J. (2017). Stable α/δ phase junction of formamidinium lead iodide perovskites for enhanced near-infrared emission. Chem. Sci. *8*, 800–805. https://doi.org/10.1039/C6SC03542F.

73. Feeney, T., Hossain, I.M., Gharibzadeh, S., Gota, F., Singh, R., Fassl, P., Mertens, A., Farag, A., Becker, J.-P., Paetel, S., et al. (2022). Four-Terminal Perovskite/Copper Indium Gallium Selenide Tandem Solar Cells: Unveiling the Path to >27% in Power Conversion Efficiency. Sol. RRL *6*, 2200662. https://doi.org/10.1002/solr.202200662.

74. Blum, M., Weinhardt, L., Fuchs, O., Bär, M., Zhang, Y., Weigand, M., Krause, S., Pookpanratana, S., Hofmann, T., Yang, W., et al. (2009). Solid and liquid spectroscopic analysis (SALSA)–a soft x-ray spectroscopy endstation with a novel flow-through liquid cell. Rev. Sci. Instrum. *80*, 123102. https://doi.org/10.1063/1.3257926.

75. Fuchs, O., Weinhardt, L., Blum, M., Weigand, M., Umbach, E., Bär, M., Heske, C., Denlinger, J., Chuang, Y.-D., McKinney, W., et al. (2009). High-resolution, high-transmission soft x-ray spectrometer for the study of biological samples. Rev. Sci. Instrum. *80*, 063103. https://doi.org/10.1063/1.3133704.

76. Weinhardt, L., Hauschild, D., Steininger, R., Jiang, N., Blum, M., Yang, W., and Heske, C. (2021). Sulfate Speciation Analysis Using Soft X-ray Emission Spectroscopy. Anal. Chem. *93*, 8300–8308. https://doi.org/10.1021/acs.analchem.1c01187.

77. Giannozzi, P., Baroni, S., Bonini, N., Calandra, M., Car, R., Cavazzoni, C., Ceresoli, D., Chiarotti, G.L., Cococcioni, M., Dabo, I., et al. (2009). QUANTUM ESPRESSO: a modular and open-source software project for quantum simulations of materials. J. Phys. Condens. Matter *21*, 395502. https://doi.org/10.1088/0953-8984/21/39/395502.

78. Grimme, S., Antony, J., Ehrlich, S., and Krieg, H. (2010). A consistent and accurate ab initio parametrization of density functional dispersion correction (DFT-D) for the 94 elements H-Pu. J. Chem. Phys. *132*, 154104. https://doi.org/10.1063/1.3382344.